Operational Analysis of a Small-Capacity Cogeneration System with a Gas Hydrate Battery

Corresponding author: Shin'ya Obara

Power Engineering Laboratory, Department of Electrical and Electronic Engineering,

Kitami Institute of Technology,

Koen-cho 165, Kitami, Hokkaido 090-8507, Japan

obara@mail.kitami-it.ac.jp

phone/FAX +81-157-26-9262

Yoshinobu Kikuchi

Power Engineering Laboratory, Graduate School of Electrical and Electronic Engineering, Kitami Institute of Technology

Kyosuke Ishikawa

Power Engineering Laboratory, Graduate School of Electrical and Electronic Engineering, Kitami Institute of Technology

Masahito Kawai

Department of Mechanical Engineering, Ichinoseki National College of Technology

Takanashi Hagishyo, Ichinoseki, Iwate 021-8511, Japan.

Yoshiaki Kashiwaya

Graduate School of Energy Science, Kyoto University

Yoshidahonmachi, Kyoto Sakyo-ku, Kyoto 606-8501, Japan

Abstract

In a cold region during winter, energy demand for residential heating is high and energy saving, the discharge of greenhouse gases, and air pollution are all of significant concern. We investigated the fundamental characteristics of an energy storage system with a Gas Hydrate Battery (GHB) in which heat cycle by a unique change in state of gas hydrate operates using the low-temperature

ambient air of a cold region. The proposed system with the GHB can respond to a high heat to power ratio caused by a small-scale cogeneration system (CGS) that is powered by a gas engine, a polymer electrolyte fuel cell, or a solid oxide fuel cell. In this paper, we explain how the relation between fossil fuel consumption and heat to power ratio of the different types of systems differ. We investigated the proposed system by laboratory experiments and analysis of the characteristics of power load and heat load of such a system in operation in Kitami, a cold district in Japan. If a hydrate formation space of 2 m^3 is introduced into the proposed system, 48% to 52% (namely, power rate by green energy) of total electric power consumption is supplied by the GHB.

Keywords: CO_2 hydrate, Gas engine, Cogeneration, Distributed Energy System, Fuel Cell.

1. Introduction

In Japan, systems for residential space heating commonly used at the present time include heating by a kerosene stove, a kerosene boiler, an air source heat pump, a geothermal heat pump, an electric storage heater, or an electric water heater [1–3]. Natural gas is now widely available in urban areas, however, and its use for space heating and home electricity production is expected to expand in the future [4–6]. In winter, energy demand for heating is high and energy saving, greenhouse gas emissions, and air pollution are serious concerns [7–9]. Therefore, the need for clean energy systems that can respond to the demand with a high heat to power ratio is apparent. Introduction of small-scale cogeneration systems (CGSs) suitable for an individual dwelling is progressing in Japan, and use of small systems powered by a gas engine, a polymer electrolyte fuel cell (PEFC), or a solid oxide fuel cell (SOFC) has spread [10–13]. However, because the different types of standard CGS described above provide only 30% to 40% of the electricity demand, they are always interconnected with a commercial power system. When an interconnected CGS is introduced, it is necessary to pay fee of commercial electric power, and fuel charge of the CGS. Considering the entire electric power system, the improvement in economic efficiency and decrease in environmental impact by the introduction of small-scale CGSs for residences has, up to this point, been limited. Moreover, operation of a basic CGS during winter does not indicate that no additional space heating is required, because the heat demand cannot be filled only with exhaust heat of the small-scale CGS. Therefore, another high capacity heat source is required. Heat supplied by a boiler raises environmental issues and when an electric heat pump is introduced into the system, a CGS with twice the conventional capacity is required. Therefore, in this paper, the heat transfer characteristics of gas-hydrate generation and dissociation characteristics by plate heat exchangers, and a miniaturization of a gas-hydrate tank by increase in the generation rate of gas-hydrate using a catalyst are newly investigated by analysis and experiment.

In this study, we propose a new distributed energy system with a Gas Hydrate Battery (GHB). In the GHB, heat cycle by a unique change in state of gas hydrate is employed, which is driven by a temperature gradient between the outside temperature of a cold region and geothermal heat. The unique change in state of a gas hydrate is as a result of the phase equilibrium state of

formation and dissociation of the gas hydrate, which produces large differential pressures in response to small temperature changes. For example, when CO_2 hydrate changes from 0 ℃ to 10 ℃, the phase equilibrium curve of formation and dissociation shows that the difference in pressures is approximately 3 MPa. Thus, if the pressure of the dissociation (that is, the expansion of the gas hydrate) is transferred to an actuator, a large power transfer can be realized by a small difference in temperature. Because gas hydrate is easy to store, its heat cycle can be used as accumulation-of-electricity equipment by combining it with an actuator, thus forming a GHB.

In this paper, we propose a small-scale hybrid CGS and GHB system to provide for all the electricity and heat requirements for an individual house in a cold region; the proposed system is not connected to a commercial power system. Furthermore, we evaluate the equipment required and assess the capacity of the system. When the ambient winter air (low-temperature side) and geothermal heat (high-temperature side) are used as heat sources for the GHB, the energy supplied by the GHB increases with increasing rate of green energy supplied to individual houses. However, because of the output characteristics of electric power and the heat change with different types of power for the small-scale CGS (a gas engine, a PEFC, or an SOFC), it is necessary to clarify the relation between each power source, and the operational methods and equipment capacity. The objective of this paper is to clarify how the installation of a hybrid distributed energy system in a house would affect fossil fuel consumption. The hybrid energy system consists of a small-scale CGS powered by a gas engine, a PEFC, or an SOFC paired with a GHB. We consider both the method of operation of the system and the relation between the heat to power ratio and fossil fuel consumption. Furthermore, we propose a new distributed energy system based on the results of the investigation described above that would contribute to solving serious problem concerning energy use, discharge of greenhouse gases, and air pollution in the winter, along with providing a high heat to power ratio.

2. System Configuration

2.1 System Scheme

Figure 1 (a) shows a conventional CGS for individual houses by cogeneration, a heat storage tank, and a geothermal heat pump using a small gas engine. The variables q_f, p, and h in Fig.

1 represent fuel flow rate based on the calorific value of the fuel, electricity, and heat, respectively; η, T, and COP represent efficiency, temperature, and coefficient of performance of the heat pump, respectively. θ_{cgs} denotes heat to power ratio of the output of the CGS, and H_{st} denotes heat storage amount. Figure 1 (a) is described in further detail below, and Fig. 1 (b) shows a system with GHB (proposed system). Power sources for the CGS can be a gas engine, a PEFC, or an SOFC. Although CO_2 hydrate is used in the proposed system, the freezing point is required of the low temperature side in this case. Therefore, the proposed system is a distributed system for introducing into a cold region. On the other hand, the high temperature heat source 10 ℃ or more by low temperature exhaust heat, renewable energy, geothermal heat, etc. is required. Moreover, this paper examines a small-scale system introduced into individual houses. Figure 2 shows the power generation efficiency, thermal power efficiency, and heat to power ratio for CGSs powered by a gas engine, a PEFC, or an SOFC [14–16]. Each power source shown in Fig. 2 is the data obtained from the experimental results.

The low-temperature heat source for the GHB shown in Fig. 1 (b) is the ambient winter air and the high-temperature heat source is the geothermal heat. High-pressure CO_2 and water are sealed in an airtight container of the GHB. The formation and dissociation of gas hydrate (equivalent to the electric charge and discharge processes of a conventional battery, respectively) are repeatable by cooling and heating this fluid. The dashed-line arrowhead in Fig. 1 (b) represents the dissociation of gas hydrate. $h_{amb,ghb,t}$ in the figure represents low-temperature ambient winter air and ambient temperature, $T_{amb,t}$, is assumed to be 0 ℃ or lower. $h_{gth,t}$ and $h_{gth,ghb,t}$ in Figs. 1 (a) and (b) are heat obtained from a geothermal heat exchanger, and $T_{gth,t}$ assumes 10 ℃ to 15 ℃; t denotes sampling time.

In both the basic and proposed systems, heat is supplied to the demand side by exhaust heat from a CGS and thermal power from a geothermal heat pump. Although the electricity output of a basic system is only from the CGS, the proposed system adds output to the demand side from the GHB. Operation of load following by the CGS is not set up; the operation of the CGS is considered to provide a constant output on a representative day of every month. Moreover, surplus power for every sampling time is stored after the change of power into heat by the geothermal

heat pump. The house used in our calculations is assumed to be airtight and thermally insulated, and space heating is considered to operate for 24 h.

2.2 Energy Flow and Energy-balance Equations

2.2.1 Basic System (Fig. 1 (a))

When fuel $q_{f,t}$ is supplied to the basic system, $p_{cgs,t}$ will be generated in the CGS. This electricity is supplied to the demand side $p_{demand,t}$, namely, to the geothermal heat pump $p_{ghp,t}$, and the heat-medium circulating pump $\Delta p_{pump,t}$ (Eq. (1)). Although heat is exchanged using a heat-medium circulating pump between the geothermal heat exchanger and the GHB, power consumption $\Delta p_{pump,t}$ in the pump in this case is calculated by Eq. (2). ρ_{hm}, $Q_{hm,t}$, η_{pump}, and L in Eq. (2) represent the density of the heat medium, the volumetric flow, the pump efficiency, and the total head (the sum of the actual head and loss head), respectively. Exhaust heat $h_{cgs,t}$ from the CGS and thermal power $h_{ghp,t}$ from the heat pump are stored in a heat storage tank, $H_{st,t}$. Moreover, the heat output of the CGS, $h_{cgs,t}$, is calculated by Eq. (3) using the CGS heat to power ratio, θ_{cgs}. Heat balance of the system is calculated by Eq. (4) using the heat $H_{st,t}$ from the heat storage tank. When heat $h_{hst,t}$ is removed from the heat storage tank and supplied to the demand side, as shown in Eqs. (5) and (6), the thermal power $h_{st,t}$ of the system is calculated by multiplying $h_{hst,t}$ by the efficiency of heat storage $\eta_{hst,t}$. The heat amount demanded, $h_{demand,t}$, is equal to $h_{st,t}$, described above. Thermal power $h_{ghp,t}$ from the heat pump is obtained from $COP_{ghp,t} \cdot p_{ghp,t}$ by supplying electricity $p_{ghp,t}$ to the heat pump (Eq. (7)).

$$\frac{1}{\theta_{cgs,t}+1} \cdot q_{f,t} = p_{cgs,t} = p_{demand,t} + p_{ghp,t} + \Delta p_{pump,t} \tag{1}$$

$$\Delta p_{pump,t} = \frac{\rho_{hm} \cdot g \cdot Q_{hm,t} \cdot L}{\eta_{pump}} \tag{2}$$

$$h_{cgs,t} = \frac{\theta_{cgs,t}}{\theta_{cgs,t}+1} \cdot q_{f,t} \tag{3}$$

$$h_{cgs,t} + h_{ghp,t} = h_{hst,t} + H_{st,t} \tag{4}$$

$$h_{st,t} = \eta_{hst,t} \cdot h_{hst,t} \tag{5}$$

$$h_{demand,t} = h_{st,t} \tag{6}$$

$$h_{ghp,t} = COP_{ghp,t} \cdot p_{ghp,t} = h_{gth,t} + p_{ghp,t} \tag{7}$$

2.2.2 Proposed System (Fig. 1 (b))

Because electricity from the proposed system is generated by both the CGS ($p_{cgs,t}$) and the GHB ($p_{ghb,t}$), balance electricity is expressed by Eq. (8). Because the amount of electric discharge from the GHB depends on the dissociation temperature of the gas hydrate, a function expressing that dependency, $\psi(T_{ghb})$, is introduced. The amount of electric discharge from the GHB is derived from Eq. (9) using the heat from the geothermal heat exchanger, $h_{gth,ghb,t}$, as an input. The dashed-line arrowhead in Fig. 1 (b) represents the charging operation of the GHB. To charge the GHB, CO_2 hydrate is formed by cooling the GHB fluid with energy, $h_{amb,ghb,t}$, taken in from ambient air with a radiator.

$$\frac{1}{\theta_{cgs,t}+1} \cdot q_{f,t} = p_{cgs,t} + p_{ghb,t} = p_{demand,t} + p_{ghp,t} + \Delta p_{pump,t} \tag{8}$$

$$p_{ghb,t} = \psi\left(T_{ghb}\right) \cdot h_{gth,ghb,t} \tag{9}$$

3. Gas Hydrate Battery (GHB)

3.1 Phase Diagram of Gas Hydrate

Figure 3 is a phase diagram of the CO_2 hydrate [17]. It shows the temperature at which water freezes at different pressures (dashed line) and the assumed "operating points" (A to C) of the GHB to be used in the proposed hybrid CGS.

For the GHB, an airtight container is filled with CO_2 and water. The initial state in the container is shown as Point A in Fig. 3. If the airtight container is cooled, the pressure and temperature of the fluid will move towards Point B shown in Fig. 3. At Point B, the water in the container starts to freeze. When the container is cooled further, the fluid will arrive at Point C. In actual use, the rate of CO_2 hydrate formation will be significantly slowed when the fluid is frozen; therefore, it is necessary to control the temperature of the heat medium carefully to attain a perfect freeze in the airtight container.

To move the fluid from Point A to Point C, the ambient air of a cold region is used as the low-temperature heat source. On the other hand, to move the fluid in the proposed system from Point C to Point A, the heat from the geothermal heat exchanger is used as the heat source. The pressure difference between Points A and C, shown in Fig. 3, can be used to operate an actuator. Because the gas hydrate is not consumed, utilization by the time shift of energy is possible similar to the case of a common battery.

3.2 GHB Scheme

Figure 4 shows the scheme of the GHB and the fluid flow paths. Figure 4 (a) shows the mode of operation during CO_2 hydrate formation (equivalent to battery charging) and Fig. 4 (b) shows the mode of operation during CO_2 hydrate dissociation (equivalent to battery discharging). The GHB consists of two sets of plate-type heat exchangers (gas hydrate generator and gas hydrate accumulator), an actuator, and a generator. The heat exchanger shown in the bottom portions of Figs. 4 (a) and (b) is the gas hydrate generator, and that shown in the upper portions is the gas hydrate accumulator. A high-pressure fluid mix of water and CO_2 is sealed in the spaces (called hydrate formation spaces) between every other set of plates in the gas hydrate generator. To heat and cool the CO_2 hydrate generating fluid, a heat medium (antifreeze solution) is filled in the other spaces between the plates. As shown in Fig. 4 (a), when cold energy is supplied to the gas hydrate generator, the mixed water and CO_2 fluid is cooled and gas hydrate is formed as shown in the phase diagram in Fig. 3. When the fluid flow shown in Fig. 4 (a) is changed to that in Fig. 4 (b) by warm temperatures supplied to the gas hydrate generator via the heat medium, the formed CO_2 hydrate shown in Fig. 4 (a) is heated within the hydrate formation space, and dissociation of CO_2

hydrate begins. When this high-pressure dissociated gas is supplied to the actuator, the system will generate electricity. The CO_2 gas from the actuator exit port will be stored in the gas hydrate accumulator. Then, when the flow of fluid shown in Fig. 4 (b) is changed to that in Fig. 4 (a), the gas hydrate formation will start again.

4. Basic Experiment

4.1 Formation Rate of CO_2 Hydrate

A previous study has shown that the rate of CO_2 hydrate formation under the best conditions is 5×10^{-3} wt%/s; 5 wt% of CO_2 hydrate is formed in approximately 17 min [18]. However, to generate gas hydrate efficiently, it is necessary to stir the CO_2–H_2O fluid vigorously. Because the formation rate will fall dramatically without stirring, a large tank of CO_2–H_2O fluid would be required to store the same energy. To lower power consumption and avoid complications with the equipment, (e.g., installation of a stirrer in a high pressure airtight container), we tried using a catalyst to improve the rate of CO_2 hydrate formation. A catalyst has been proven effective in forming methane hydrates under weak stirring conditions [19]. Following methods and procedures described by Takahata and others [19], we sintered iron oxide in an electric furnace for 24 h at a temperature of 1000 °C. Then, 50.0 g of the iron oxide and 14.3 g of graphite (atomic ratio of 1:1) were milled together for 48 h. The prepared catalyst with a concentration of 0.5 wt% was mixed in the test space of the basic experimental apparatus (for details, the next section describes.).

4.2 Basic Experiment of Change in State of CO_2 Hydrate

Figure 5 shows the basic experimental apparatus for investigating the characteristics of formation and dissociation of CO_2 hydrate. As shown in the figure, the test equipment consists of a double tube heat exchanger, and a heat medium used for heating and cooling is pumped through the inner tube. The space between the outer and inner tubes (called the test space) is filled with a mixture of pure water and CO_2, the material for a gas hydrate. The volume of this test space is approximately 100 cm^3. The outer and inner diameters of the outer tube are 25.4 mm and 21.2 mm, respectively, and those of the inner tube are 12.8 mm and 10.2 mm, respectively; the test space is approximately 370 mm in length. The experimental apparatus is miniaturized as much

as possible from maintaining a uniform system and preventing the influence of disturbance. The formation or dissociation of CO_2 hydrate occurs in the test space. Temperature sensors (T type thermocouple) are installed on the outer wall of the outer tube and at the entrance of the heat medium, and each temperature is recorded. Furthermore, pressure in the test space is measured by pressure sensors (piezoelectric device type).

4.3 Experimental Procedure

Although the half of the capacity of the test space is satisfied with filled with a mixture of pure water and CO_2, because it takes a long time to dissolve CO_2 in water and it is necessary to fully dissolve CO_2 in the water before the experiment begins, the first several hours of each experimental run is a preparation period for dissolving CO_2. When cooling water flows into the inner tube, gas hydrate is generated in the test space, and on the other hand, when warm water flows in, dissociation of gas occurs. The heat cycle of gas hydrate can be examined by supplying the heat medium of low temperature and warm temperature to the inner tube alternately.

5. Compound Energy System for Cold Region Houses

Figure 6 is a scheme of an energy system for cold region houses using the different cogeneration equipment and the GHB considered in this paper. Figure 6 (a) is a scheme of the GHB and heat pump, Fig. 6 (b) shows the outline of two slightly different small-scale CGSs, and Fig. 6 (c) shows a system controller. In Fig. 6 (a), to charge the GHB (for gas hydrate formation), the cold ambient air is taken in through Radiator (2). The heat medium from the geothermal heat exchanger is at a temperature of 15 ℃, and after flowing through the gas hydrate generator, it is output at 10 ℃. Next, the heat medium is supplied to a heat exchanger and then passed on to the heat pump. When the low-temperature side of the system (evaporator side) is at 8 °C, the high-temperature side (condenser side) can attain a temperature of 45 ℃ using a heat pump presently available as a commercial product in Japan; the COP of this system would be approximately 4.6 [20].

6. GHB Heat Exchanger Specifications

Figure 7 shows a heat transfer model of the GHB. Figures 7 (a) and (b) show the formation and dissociation of CO_2 hydrate, respectively. The heat medium is circulated through the heat exchangers by a pump, and each flow velocity is denoted by v_{hmc} and v_{hmw}. By introducing v_{hmc} or v_{hmw} into the Reynolds number, Re_{hmc}, in the path of the heat medium, the rate of the forced convection heat transfer is calculated from Eq. (10) [21]. Although the hydrate formation space is filled with CO_2 saturated water and CO_2 gas, CO_2 gas still flows into the hydrate formation space during formation and flows out during dissociation. Moreover, the CO_2 saturated water is liquid, whereas the CO_2 gas hydrate is a viscous slurry. Therefore, the natural convective heat transfer represented by Eq. (11) is applied to the hydrate formation space [22]. The formation and dissociation of CO_2 hydrate shown in Figs. 7 (a) and (b) can be represented by Eqs. (12) and (13), respectively. Subscripts s, l, and li in Eqs. (12) and (13) denote the sensible heat of CO_2 saturated water containing CO_2 hydrate in the hydrate formation space, the reaction heat of the formation or dissociation of CO_2 hydrate, and the latent heat of freezing or dissolution of CO_2 saturated water frozen in the container. Eq. (14) represents the overall heat transfer coefficient for the plate heat exchangers shown in Fig. 7 (a). When this overall heat transfer coefficient is introduced into Eq. (15), the heat transferred to the CO_2 saturated water from the heat medium is calculated. Each heat transfer rate in Eq. (14) can be obtained from the Nusselt number (Nu) in Eqs. (10) and (11). The heat transferred from the heat medium to CO_2 saturated water is calculated based on the model of Fig. 7 (b). as well as Eqs. (14) and (15). Because the flow velocities (v_{hmc}, v_{hmw}) and the heat transfer areas (S_{ghf}, S_{ghd}) in the path of the heat medium are obtained from Eqs. (10) through (15), the specifications of the GHB heat exchanger and the flow rate of a heat-medium circulating pump can also be calculated.

However, compressibility of gas and detail of the flow of fluid are not taken into consideration by the system shown in Fig. 7. The handling of the fluid described in the top causes an analysis error. Moreover, in the variables of the analysis used in this paper, the heat transfer analysis shown in Fig. 7 is expected to influence in analytic accuracy strongly. Although a heat transfer amount is calculated by Eqs. (10) to (15), because the change of state by formation or dissociation of gas-hydrate is a slow reaction, the change of state is not taken into consideration in these equations. In order to raise analytic accuracy, it is necessary to investigate the detailed relation

of formation and dissociation of gas-hydrate and heat transfer amount by many fundamental experiments.

$$\mathrm{Nu}_{hmc} = 0.037 \cdot \mathrm{Pr}_{hmc}^{1/3} \cdot \mathrm{Re}_{hmc}^{4/5} \tag{10}$$

$$\mathrm{Nu}_{ghf} = 0.021 \cdot \left(\mathrm{Gr}_{ghf} \cdot \mathrm{Pr}_{ghf}\right)^{0.4} \tag{11}$$

$$q_{ghf} = q_{ghf,s} + q_{ghf,l} + q_{ghf,li} \tag{12}$$

$$q_{ghd} = q_{ghd,s} + q_{ghd,l} + q_{ghd,li} \tag{13}$$

$$K_{hmc,ghf} = \frac{1}{1/h_{hmc} + \delta/\lambda + 1/h_{ghf}} \tag{14}$$

$$q_{ghf} = K_{hmc,ghf} \cdot S_{ghf} \cdot \Delta T_{hmc,ghf} \tag{15}$$

7. Analysis Method

7.1 Analysis Conditions

7.1.1 Outside Temperature

As a test case of the proposed system for a cold region in Japan, we used outside temperature data for the city of Kitami, Hokkaido Prefecture, Northern Japan for the period between November 2012 and March 2013 (Fig. 8). Freezing temperatures are not usually observed in Kitami between April and November (spring, summer, and autumn); therefore, CO_2 hydrate formation is difficult during that time. For this reason, operation of a GHB in Kitami is only feasible in the period from December to March.

7.1.2 Energy Demand

Figure 9 shows power load (Fig. 9 (a)) and heat load (Fig. 9 (b)) for a hypothetical individual house used in this analysis. Each load pattern shown in Fig. 9 represents one day of power usage and was prepared using data from a study that dealt with energy utilization in Kitami [23]. Because both cooling and heating are included in heat load, the total power loads (including heating and cooling household appliances, lights, computers, among others) for each month are

fairly similar. The average heat to power ratio of February representative days is 15.9, as shown by Fig. 9. Although electricity is supplied so that the power load shown in Fig. 9 (a) can be met by the proposed system, the output from both the basic and proposed systems is set as a constant on a representative day, as shown by the broken line in Fig 9 (a). Using the sampling time (hatching region) during which the electricity production (dashed line) by the CGS exceeds the power load in Fig. 9 (a), surplus power is changed into heat via the heat pump and that heat is stored. However, the sum total of the exhaust heat from the CGS and the thermal power provided by the heat pump during each sampling time is constrained to be less than the heat demand (it is the total heat for a representative day every month shown in Fig. 9 (b)) on any representative day. The fixed electricity output of the CGS shown in Fig. 9 (a) is determined. Space heating is always supplied to the demand side through a heat storage tank assuming 24-h supply in an airtight thermally insulated house.

7.2 Flow Analysis

Figure 10 shows the analysis flow of the operation of a small-scale CGS paired with a GHB installed in a house in a cold region and the proposed system. A letter, (a) through (o), is assigned to each block in the figure. Different types of initial values and data for analysis are used as input for Block (a). The data entered into Block (a) are the characteristics of each power source (Fig. 2), such as the temperature–pressure characteristics of gas hydrate (Fig. 3), the temperature of the geothermal heat exchange (Fig. 6), the ambient air temperature (Fig. 8), the load pattern of electricity and heat (Fig. 9), the COP table of the heat pump [20] and pump efficiencies (= 0.75), the total head of the pump (L = 20 m), the freeze rate of hydrate formation space (= 20%), and the heat storage loss (= 10%). System operation is analyzed by changing the capacity of the hydrate formation space (loop between Blocks (b) and (o)), and the rated power of the CGS (Block (c)). Although the repetition pattern of accumulation of electricity and electric discharge of the GHB is specified before the calculation begins and entered into Block (d), the electric charge (gas hydrate formation) and electric discharge (gas hydrate dissociation) are repeated every 3 h in the calculation. The repetition of Blocks (e) to (l) is a loop of the sampling time during a representative day, and Blocks (f) through (k) represent calculation of power and heat balances described in

Section 2.2. The fuel consumption of the CGS is calculated from Eq. (1) or Eq. (8) in Block (m). However, because the power source of the CGS has a fixed output, the load factor is calculated from this set power and the load for each sampling time. The power generation efficiency of the power source and the efficiency of thermal power are obtained using the load factors from Fig. 2. To determine which configuration results in minimum fuel consumption by the CGS, the conditional branch from Block (n) returns the calculation to Block (c) and the CGS output is adjusted. Loop (e) to (l) is then recalculated. The calculations summarized in Fig. 9 allow us to resolve the relation between the rated power of the CGS and capacity of the hydrate formation space, the fuel consumption, and the optimum operational conditions for each piece of equipment.

8. Results and Discussion

8.1 Results of CO_2 Hydrate Experiments

Figure 11 shows the results of the hydrate formation and dissociation experiment described in Section 3 and illustrated by Fig. 5. Figure 11 shows the results for experimental runs during which the heat medium, initially at a temperature of 20 °C, was cooled to −5 °C and then heated to 30 °C to first form and then dissociate CO_2 hydrate. Figure 11 (a) shows the results of the run with no catalyst and Fig. 11 (b) shows the experimental result with the iron oxide–carbon catalyst described in Section 4.1. Note the change in shape of pressure curves between the 1.0 and 1.5 h marks. The formation rate with the catalyst, approximately 30 min (Fig. 11 (b)), is clearly much faster than that of CO_2 hydrate formation without the catalyst, which is approximately 2 h (Fig. 11 (a)). Based on these results, it seems that the formation and dissociation of CO_2 hydrate can be repeated in the GBH of the proposed system.

8.2 System Operation

8.2.1 Power Balance Analysis Results

Figures 12–15 show the results of operational analysis for the conventional (Fig. 12) and proposed system (Figs. 13–15) for the representative days in November and February. The results were calculated for the balance of electricity and heat according to the flow analysis shown in Fig. 10. In each figure (a) in Figs. 12 through 15, the “Output of CGS” value shown is a set value of

output power. Although the set value of output for a power source is obtained for the representative day of each month, the value of the largest output for the representative day of each month is chosen on the basis of the rated power of the CGS (i.e., the capacity of the generator). A load factor is obtained from the rated power (which was predetermined) and the load for every sampling time of all the representative days. These load factors are then referenced to Fig. 2 and the power generation efficiency of each power source and the efficiency of thermal power are obtained from that figure.

Although Figs. 13–15 show the results of the operational analysis of the proposed system, because outside temperature was high on the representative day in November, the GHB in the proposed system would not charge for that period as shown in (a) of each figure. As shown in the analysis results of electricity in February shown in Figs. 13 (a)-15 (a), the output power of each power source in February by the proposed system is large in order of SOFC, PEFC, and gas engine. The order described in the top is the magnitude of exhaust heat (from Fig. 2), and the operation result by a heat load following operation is outputted as analysis solution. If the capacity of hydrate formation space is increased, the output power of each power source can be reduced relatively. If hydrate formation space of 2 m^3 is installed in the system using gas engine, a PEFC, SOFC, the fall of 33 %, 38 %, and 39 % of power output (reduction of fuel cost) can be realized, respectively. When the capacity of the hydrate formation space is set up in 4 m^3, the power output of each power source will further drop.

When 20% of the CO_2 saturated water in the volume of the hydrate formation space shown in Fig. 7 is frozen, power to the heat-medium circulating pump, which is unavoidably produced by the GBH, reaches approximately 1.5 times that supplied to the geothermal heat pump. Therefore, when the outside ambient air becomes extremely cold, it is necessary to decrease the electric power consumption of the heat-medium pump to avoid the freezing of the CO_2 saturated water in the gas hydrate generator.

8.2.2 Heat Balance Analysis Results

Surplus power is changed into heat by the heat pump and this allows the power balance equations shown in Eqs. (1) and (8) to be completed as shown in each figure (b) of Figs. 12 through 15. As shown in Figs 13(b)-15 (b), the thermal power of heat pump is small in order of a gas engine,

PEFC, and SOFC. The order described in the top is the magnitude of the exhaust heat of each power source. Therefore, selection of the optimal power source introduced into the proposed system is strongly influenced in the heat to power ratio of a demand side. The output of the heat pump changes each time. The output fluctuations of the heat pump can supply stable heat by passing heat from the storage tank to the demand side.

8.3 Power Generation Efficiency and Fuel Consumption

Figure 16 shows the results of calculations for the load factor, the power generation efficiency, and the fuel consumption during each representative day of every month for the basic system. Moreover, Fig. 17 shows calculated results for the same three parameters for the proposed system with a GHB, a set of graphs for each of the proposed CGSs powered by a gas engine, a PEFC, or an SOFC. The load factor in the basic system is high in winter (December, January, and February) when the outside air temperature is low; the load factor decreases in November and March owing to a reduction in heat load.

Concerning the proposed system, the load factor for each different power source, with 0 m^3 capacity of the hydrate formation space, will be high in December, January, and February and low in November and March. However, increasing the capacity of the hydrate formation space will reduce all the load factors. Low temperatures reduce the load on each CGS power source because electric energy from the GHB increases in the proposed system when the outside air temperature is low. To avoid a drop in power generation efficiency when the GHB accompanied with large capacity hydrate formation space is introduced, each large capacity externally fueled power source should be replaced with a number of lower capacity units to increase the load factor. However, if this is conducted, then some mechanism of providing control for the increased number of units will be required.

In winter (December, January, and February), when the outside air temperature is low, the basic system exhibits high fuel consumption (Fig. 16 (c)). The fuel consumption will decrease in November and March because the outside air temperature is higher. The fuel consumption requirements of the basic system are dependent on the change in the heat demand. On the other hand, the GHB generates power using green energy and the fuel consumption of the proposed

system decreases with increasing hydrate formation space (right column of panels in Fig. 17). Note that the SOFC CGS with 0 to 3 m^3 capacity of hydrate formation space has the lowest fuel consumption (light blue, orange, gray, and yellow bars), and PEFC becomes more advantageous when the hydrate formation space is 4 m^3 (dark blue bar). The reason for this is that operating the SOFC at low load factors results in a large drop in power generation efficiency. If one is considering introducing a high capacity GHB with a large hydrate formation space into an SOFC CGS, one must consider the possibility of aggravating fuel consumption. Our results, in the right column of panels in Fig. 17, showed that the proposed system significantly reduced fuel consumption during winter in a cold region.

8.4 Utilization Rate of Renewable Energy

Figure 18 shows the source of the energy for the representative days using the basic system and Fig. 19 shows sources for the proposed systems. Figure 19 shows that as power supplied by the GHB increases (because of increased hydrate formation space), the electricity output by the CGS decreases. For example, the percentage of electricity provided by the GHB in the proposed system accompanied with a hydrate formation space of 2 m^3 is 48% to 52%, whereas a GHB with a hydrate formation space of 4 m^3 provides 60% to 80% of the electricity.

In the basic system, the proportion of the output by the heat pump is 40% to 44%. The percentages of output by the heat pump of the gas engine CGS, the PEFC CGS, and the SOFC CGS in the case of 0 to 3 m^3 of hydrate formation space in the proposed system are 44% to 80%, 57% to 87%, and 76% to 91%, respectively. In the case of 4 m^3 of hydrate formation space, the percentages of output provided by the heat pump reach 95%, 97%, and 98%, respectively (in February). The capacity of the GHB becomes larger when the capacity of the hydrate formation space increases, and the proportion of the thermal power that can be provided by the heat pump (driven by the electricity of the GHB) increases when the ambient temperature is very low. Although the SOFC CGS is efficient at producing electricity, when an SOFC CGS with large heat to power ratio is installed in a cold region, the initial capacity of the heat pump will become large, 10% to 20%, compared with the gas engine CGS and the PEFC CGS.

8.5 Heat to Power Ratio and Fuel Consumption Relations

Figure 20 shows the relation between the heat to power ratio of the system and fuel consumption obtained from operational analysis of each system in November 2012 to March 2013 in Kitami. However, the heat to power ratios of only four of the real-world systems (two thermal power CGS + heat pump systems and to two electricity output CGS + GHB systems) match the heat to power ratio of the systems modeled in this study. The range of the heat to power ratios for the installed systems in Kitami was 3.3–5.8. Furthermore, the electricity and heat values for the gas engine CGS, the PEFC CGS, and the SOFC CGS shown in Fig. 20 were generated with different types of CGSs. Some systems had no GHB at all, whereas others included GHBs with capacities of hydrate formation spaces of up to 4 m^3. The electricity output of the GHB decreases when the capacity of hydrate formation space is small. All the systems shown in Fig. 20 with heat to power ratios of 5.0 or greater are systems without the capacity of hydrate formation space. Additionally, in the basic systems, the power to run the heat pump is only provided by the CGS. Because the electricity output in these systems increases with increasing thermal power, there are no basic CGSs with a high heat to power ratio in operation. There are also no SOFC CGSs with high system heat to power ratios. This is because power generation efficiency of the SOFC CGSs is quite high and the system produces little exhaust heat.

9. Conclusions

We investigated the fundamental characteristics of a unique type of energy storage equipment with a Gas Hydrate Battery or GHB that functions using the unique change in state of a gas hydrate. We performed laboratory experiments to test the efficiency of gas hydrate generation and also simulated the operation of a number of different systems in individual houses of a cold region in Kitami, Japan. The investigated distributed energy system, the “proposed system,” consists of small-scale CGS and GHB systems powered by a gas engine, a PEFC, or an SOFC. We reached the following conclusions:

(1) The proposed system only works in winter when the outside air temperature is less than 0 °C. However, when CO_2 saturated water in the gas hydrate generator is frozen by the ambient air, the increase in the power consumption of the heat-medium pump is large. Therefore, when

the ambient air becomes extremely cold, the uptake of ambient air must be controlled or supply to the gas hydrate generator and the geothermal pump must be changed appropriately because the water in the gas hydrate generator must not be allowed to freeze.

(2) The capacity of the GHB becomes larger when the capacity of the hydrate formation space is increased. Furthermore, the thermal power of the heat pump powered by electricity from the GHB increases in winter. For example, a heat pump in the proposed system powered by a GHB with a hydrate formation space of 0 to 3 m^3 can attain output ratios of 44% to 80%, 57% to 87%, and 76% to 91% in a system with a gas engine, a PEFC, or an SOFC, respectively. Although the SOFC CGS is advantageous for obtaining electricity, because there is little thermal power, the heat pump of large capacity is required. As a result, the capacity of the heat pump becomes large, that is, 10% to 20% of that from a gas engine or a PEFC.

(3) Because the GHB generates electricity using green energy, the fuel consumption of the proposed system decreases with increasing capacity of the hydrate formation space of the GHB. For example, a GHB in the proposed system can generate 48%–52% of the electricity with 2 m^3 capacity of hydrate formation space. If the GHB hydrate formation space is 4 m^3, electricity generation can increase to 60%–80%. Therefore, a CGS with a GHB and a high heat to power ratio in cold regions allows the utilization rate of green energy to increase and significantly reduces fossil fuel consumption.

Nomenclature

COP : Coefficient of performance

Gr : Grashof number

g : Acceleration due to gravity [m/s^2]

H_{st} : Heat storage amount [kWh]

h : Heat [kW]

h_c : Heat coefficient [$kW/(m^2 \cdot ℃)$]

K : Overall heat transfer coefficient [$kW/(m^2 \cdot ℃)$]

L : Total pump head [m]

Nu : Nusselt number

Pr : Prandtl number

p : Electricity [kW]

Δp : Electricity consumption [kW]

Q : Volumetric flow [m^3/s]

q : Quantity of heat [kW]

q_f : Calorific value of fuel [kW]

Re : Reynolds number

S : Heat transfer area [m^2]

T : Temperature [℃]

ΔT : Temperature difference [℃]

t : Sampling time [h]

v : Flow rate [m/s]

Roman character

δ : Thickness of heat transfer plate of plate heat exchangers [m]

η : Efficiency [%]

η_{hst} : Efficiency of heat storage [%]

λ : Coefficient of thermal conductivity [W/(m・℃)]

θ_{cgs} : Heat to power ratio of demand

ψ : Function depending on dissociation temperature

Subscript

amb : Ambient

cgs : Cogeneration

ghb : Gas hydrate battery

ghd : CO_2 dissolved water in gas hydrate dissociation

ghf : CO_2 dissolved water in gas hydrate formation

ghp : Geothermal heat pump

gth : Geothermal heat

hm : Heat medium

hmc : Cold heat medium

hmw : Warm heat medium

hst : Heat storage tank

l : Heat of reaction of formation or dissociation of CO_2 hydrate

li Latent heat of freezing or melting of CO_2 dissolved water

s : Sensible heat of CO_2 dissolved water

st : Output of heat storage tank

References

[1] Fujii H, Lutzenhiser L. Japanese residential air-conditioning: natural cooling and intelligent systems. Energy Build 1992;18:221–33.

[2] Goto H, Goto M, Sueyoshi T. Consumer choice on ecologically efficient water heaters: Marketing strategy and policy implications in Japan. Energy Econ 2011;33:195–208.

[3] Benli H. Energetic performance analysis of a ground-source heat pump system with latent heat storage for a greenhouse heating. Energy Convers Manage 2011;52:581–89.

[4] Ren H, Gao W. Economic and environmental evaluation of micro CHP systems with different operating modes for residential buildings in Japan. Energy Build 2010;42:853–61.

[5] Shimoda Y, Yamaguchi Y, Okamura T, Taniguchi A, Yamaguchi Y. Prediction of greenhouse gas reduction potential in Japanese residential sector by residential energy end-use model. Appl Energy 2010;87:1944–52.

[6] Shimokawa M, Tezuka T. Development of the “Home Energy Conservation Support Program” and its effects on family behavior. Appl Energy 2014;114:654–62.

[7] Zhu D, Tao S, Wang R, Shen H, Huang Y, Shen G, et al. Temporal and spatial trends of residential energy consumption and air pollutant emissions in China. Appl Energy 2013;106:17–24.

[8] Ozyurt O, Ekinci DA. Experimental study of vertical ground-source heat pump performance evaluation for cold climate in Turkey. Appl Energy 2011;88:1257–65.

[9] Barbieri ES, Melino F, Morini M. Influence of the thermal energy storage on the profitability of micro-CHP systems for residential building applications. Appl Energy 2012;97:714–22.

[10] Zuliani N, Taccani R. Microcogeneration system based on HTPEM fuel cell fueled with natural gas: Performance analysis. Appl Energy 2012;97:802–8.

[11] Wang Y, Chen KS, Mishler J, Cho SC, Adroher XC. A review of polymer electrolyte membrane fuel cells: Technology, applications, and needs on fundamental research. Appl Energy 2011;88:981–1007.

[12] Yamasaki Y, Kanno M, Suzuki Y, Kaneko S. Development of an engine control system using city gas and biogas fuel mixture. Appl Energy 2013;101:465–74.

[13] Choudhury A, Chandra H, Arora A. Application of solid oxide fuel cell technology for power generation—A review. Renewable Sustainable Energy Rev 2013;20:430–42.

[14] Wakui T, Yokoyama R. Optimal sizing of residential gas engine cogeneration system for power interchange operation from energy-saving viewpoint. Energy 2011;36:3816–24.

[15] Maeda K, Masumoto K, Hayano A. A study on energy saving in residential PEFC cogeneration systems. J Power Sources 2010;195:3779–84.

[16] Lamas J, Shimizu H, Matsumura E, Senda J. Fuel consumption analysis of a residential cogeneration system using a solid oxide fuel cell with regulation of heat to power ratio. Int J Hydrogen Energy 2013;38:16338–43.

[17] Sloan D, Koh AC. Clathrate hydrates of natural gases. New York: CRC Press; 2007.

[18] Jerbi S, Delahaye A, Fournaison L, Haberschill P. Characterization of CO_2 hydrate formation and dissociation kinetics in a flow loop. Int J Refrigeration 2010;33:1625–31.

[19] Takahata M, Kashiwaya Y, Ouchi M, Ishii K. Effect of catalyst of iron oxide-carbon on methane hydrate formation under weak stirring condition. Tetsu-to-Hagane 2006;92:393–400. (In Japanese)

[20] Homepage of Aomori Prefectural Government, Geothermal application and a hot spring exhaust hot water heat pump system by Zeneral Heatpump Industry Co., Ltd. 2014.5.7, Retrieved from https://www.pref.aomori.lg.jp/soshiki/energy/enerugi/files/handout_No.3.pdf

[21] MIT Computer Science and Artificial Intelligence Laboratory, Convection From a Rectangular Plate, 2014.5.6, Retrieved from http://people.csail.mit.edu/jaffer/SimRoof/Convection/

[22] Holman JP. Heat Transfer (McGraw-Hill Series in Mechanical Engineering). 9th ed. McGraw-Hill College: Blacklick; 2001.

[23] Narita K. The research on unused energy of the cold region city and utilization for the district heat and cooling. Ph.D. thesis 1996, Hokkaido University. (In Japanese)

Captions

Fig. 1 Schematic diagrams showing energy flow in the analyzed systems

(a) Basic system

(b) Proposed system

Fig. 2 Graphs showing efficiency and heat to power ratio of three power sources

(a) Gas engine CGS

(b) PEFC CGS

(c) SOFC CGS

Fig. 3 Phase diagram of CO_2 hydrate and system operation

Fig. 4 Gas hydrate battery system (GHB)

(a) Diagram showing CO_2 hydrate formation

(b) Diagram showing power generation by CO_2 hydrate dissociation

Fig. 5 Diagrammatic drawing of the experimental apparatus for CO_2 hydrate formation

Fig. 6 Flow diagrams for energy systems for cold region houses

(a) GHB and heat pump

(b) Cogeneration

(c) Controller

Fig. 7 Diagram showing heat transfer in a GHB

(a) CO_2 hydrate formation

(b) CO_2 hydrate dissociation

Fig. 8 Graph showing hourly air temperature for five representative days during November 2012 to March 2013 in Kitami, Japan

Fig. 9 Graphs showing electricity demand and heat load in kW versus time during one day for individual houses in Kitami

(a) Electricity load

(b) Heat load

Fig. 10 Calculation flow for analyzing the operation of a small-scale CGS paired with a GHB installed in a house in a cold region

Fig. 11 Graphs of internal pressure versus time for gas hydrate formation–dissociation experiments. The experiments tested the efficacy of adding a catalyst to the reaction space.

(a) Conventional method test without catalyst

(b) Test using iron oxide–carbon catalyst

Fig. 12 Graphs showing heat and electric load and output for a basic cogeneration power system during one day

(a) Electricity

(b) Heat

Fig. 13 Graphs showing the results from a computer simulated operation of a gas engine-powered CGS for one day

(a) Electricity

(b) Heat

Fig. 14 Analysis results of power equipment operation for PEFC CGS

(a) Electricity

(b) Heat

Fig. 15 Analysis results of power equipment operation for SOFC CGS

(a) Electricity

(b) Heat

Fig. 16 Graphs showing monthly performance of the basic system during November 2012 to March 2013

(a) Load factor

(b) Generation efficiency

(c) Fuel consumption

Fig. 17 Graphs showing total monthly load factors, generation efficiency, and fuel consumption for three types of CGSs for the period November 2012 to March 2013.

(a) Gas engine CGS

(b) PEFC CGS

(c) SOFC CGS

Fig. 18 Graphs showing the source of electric and heat energy for the five representative days for the basic CGS

Fig. 19 Composition of energy outputs by each CGS

(a) Gas engine CGS

(b) PEFC CGS

(c) SOFC CGS

Fig. 20 Relation between heat to power ratio and fuel consumption for each system. Capacity of 0 to 4 m^3 of hydrate formation space.

Fig. 1 Schematic diagrams showing energy flow in the analyzed systems

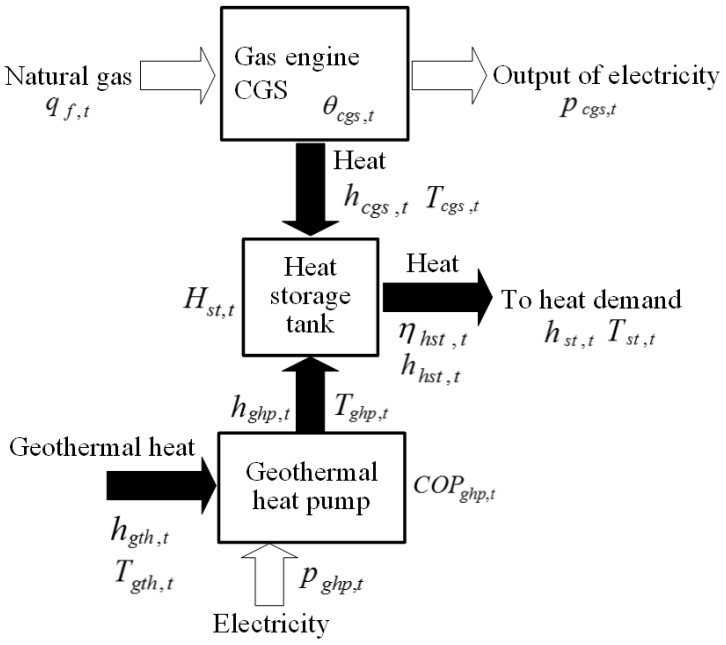

(a) Basic system

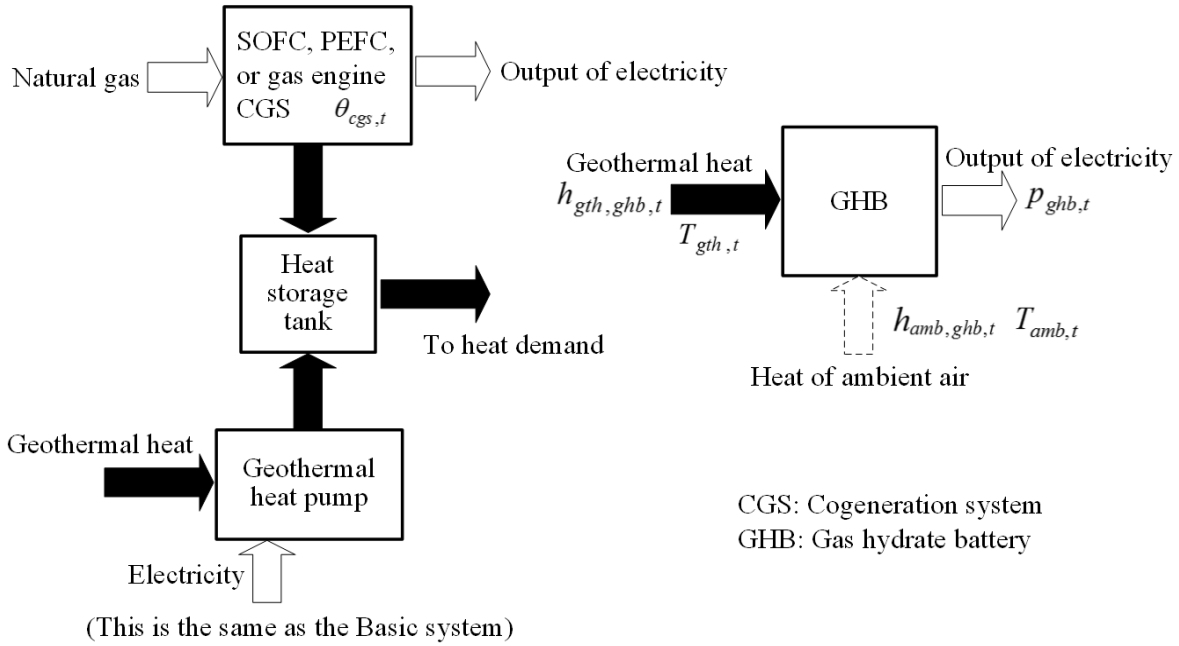

(b) Proposed system

Fig. 2 Graphs showing efficiency and heat to power ratio of three power sources

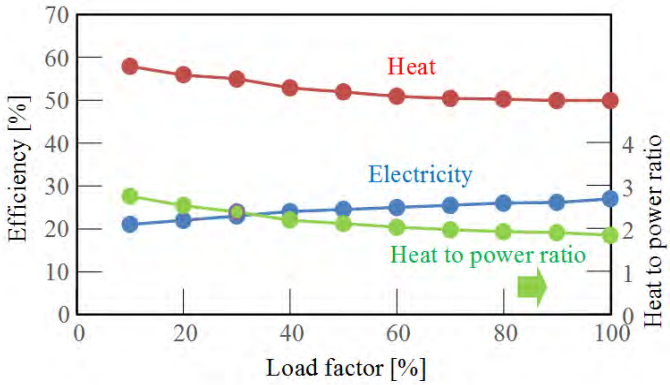

(a) Gas engine CGS

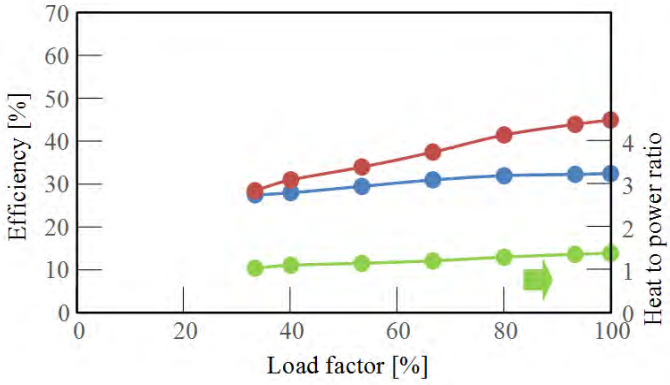

(b) PEFC CGS

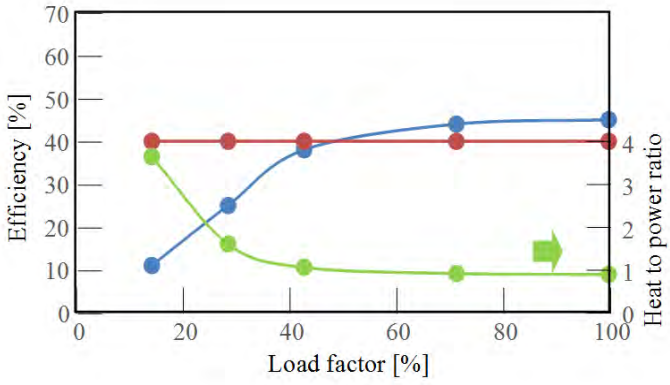

(c) SOFC CGS

Fig. 3 Phase diagram of CO_2 hydrate and system operation

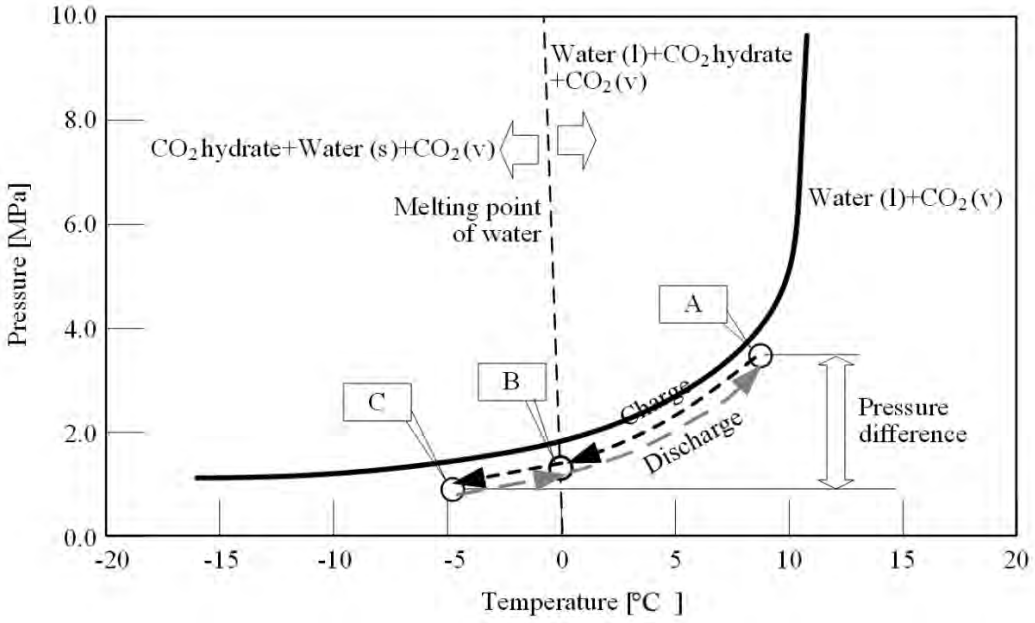

Fig. 4 Gas hydrate battery system (GHB)

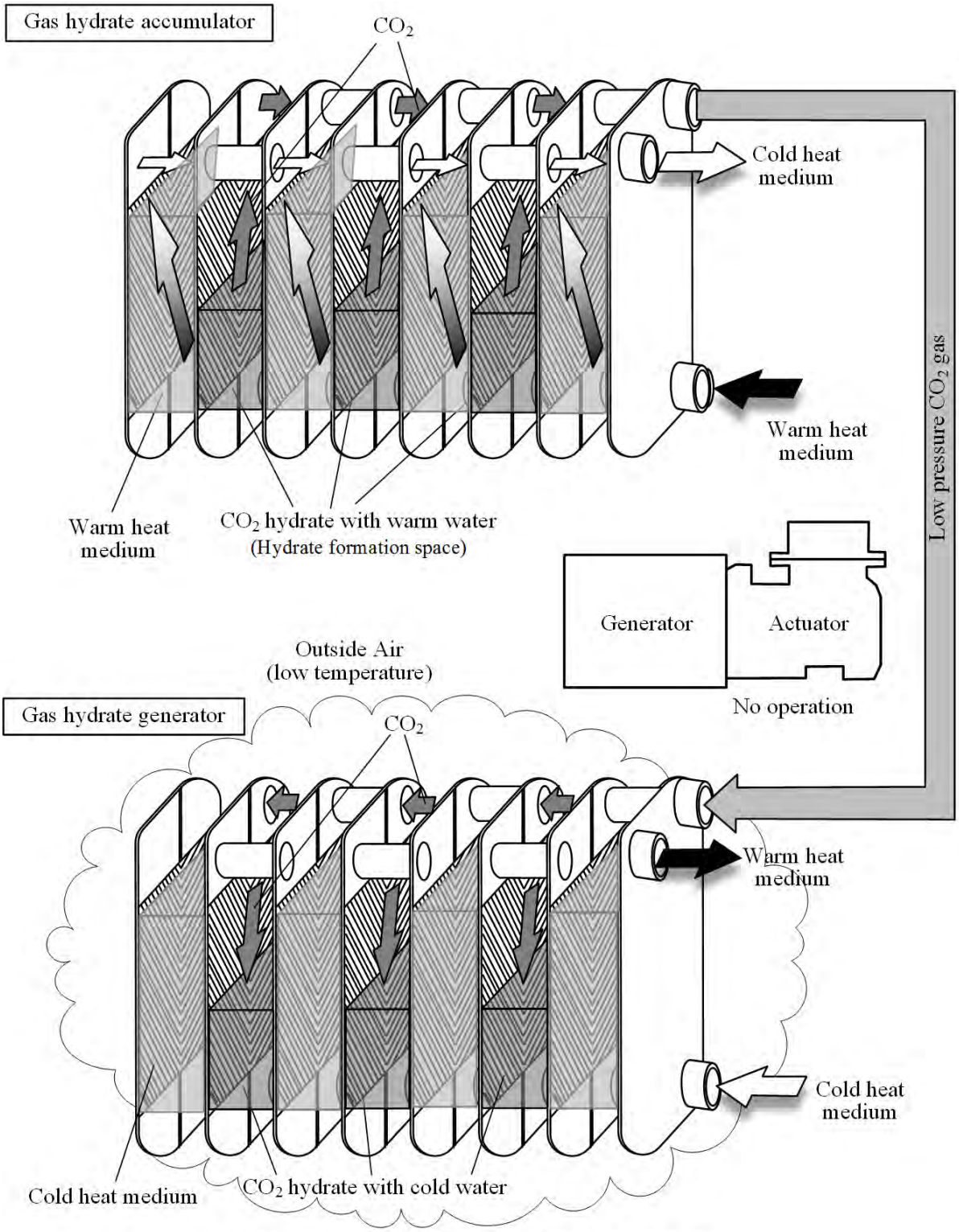

(a) Diagram showing CO_2 hydrate formation

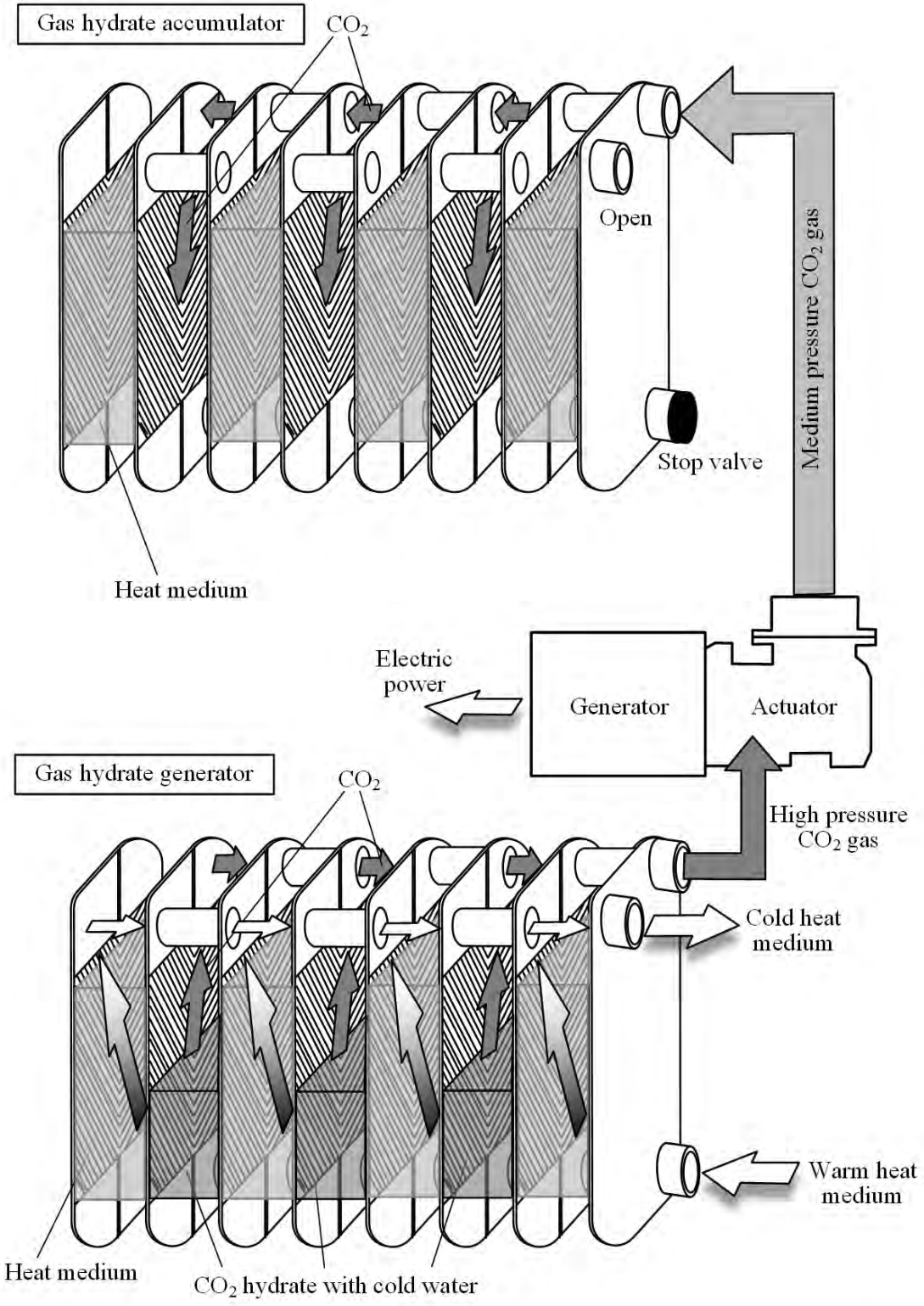

(b) Diagram showing power generation by CO_2 hydrate dissociation

Fig. 5 Diagrammatic drawing of the experimental apparatus for CO_2 hydrate formation

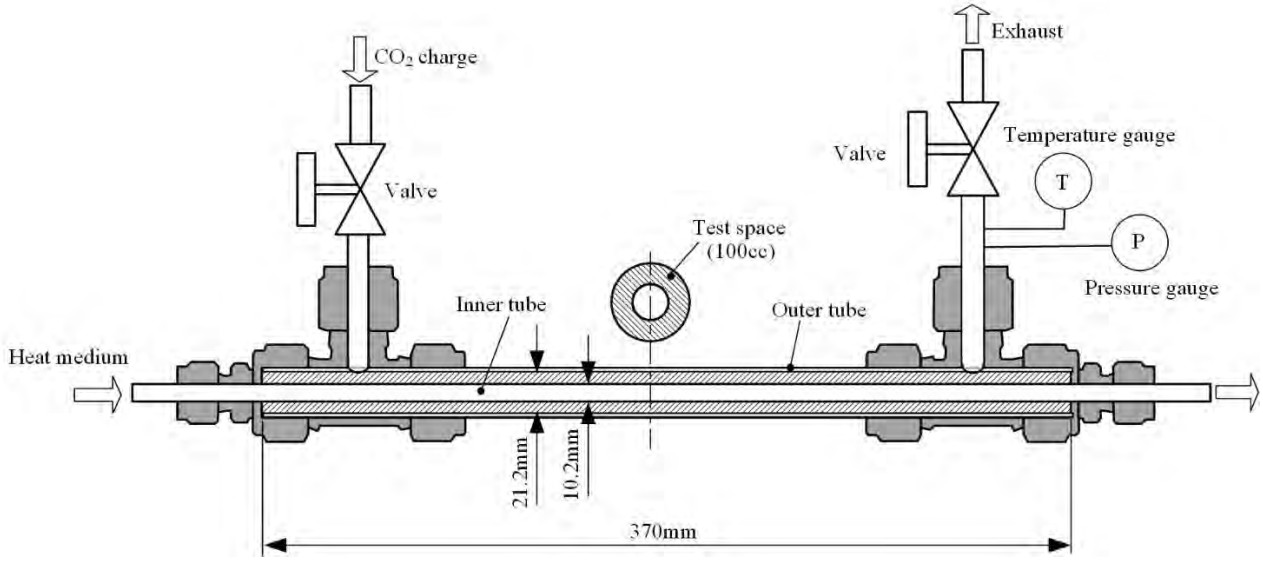

Fig. 6 Flow diagrams for energy systems for cold region houses

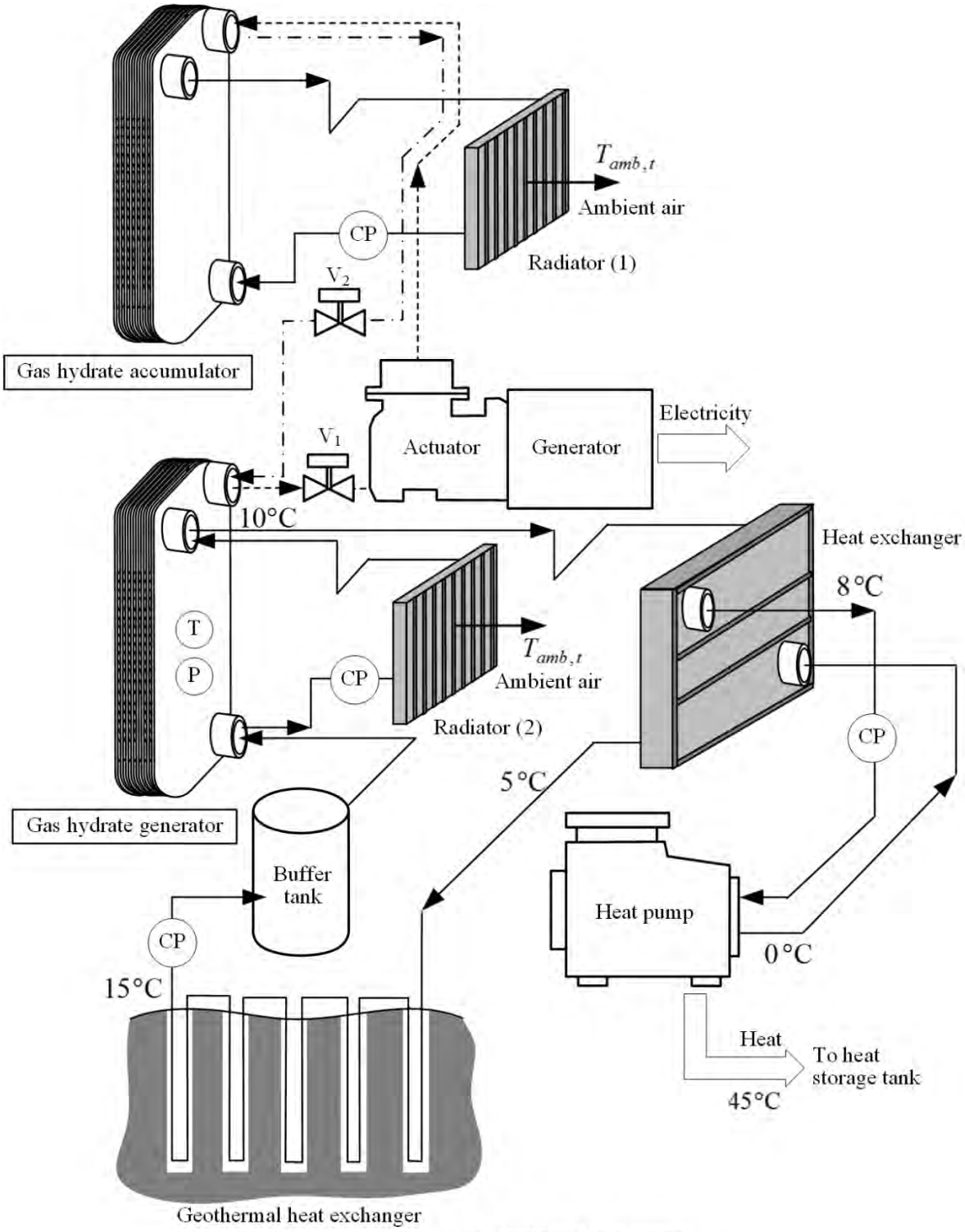

(a) GHB and heat pump

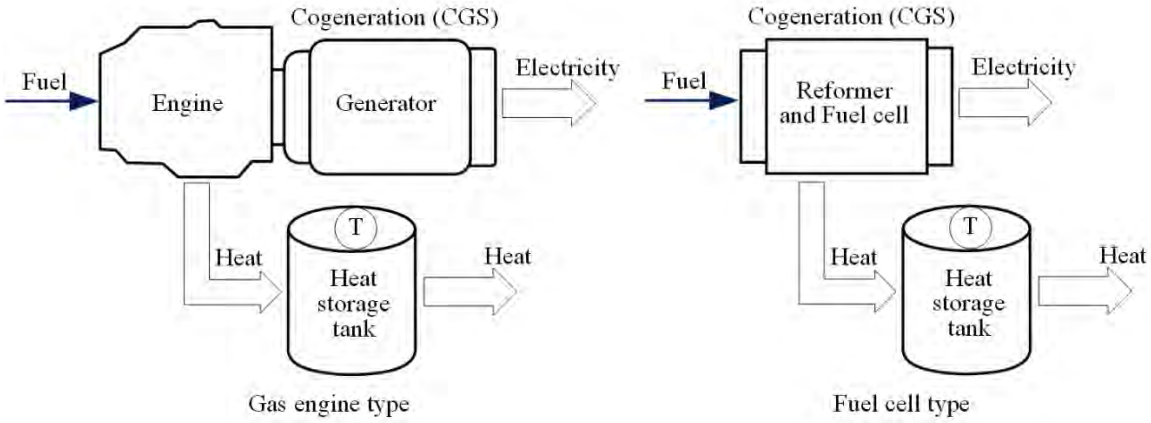

(b) Cogeneration

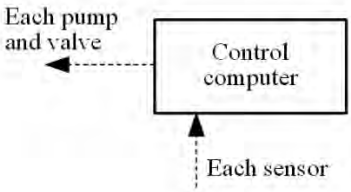

(c) Controller

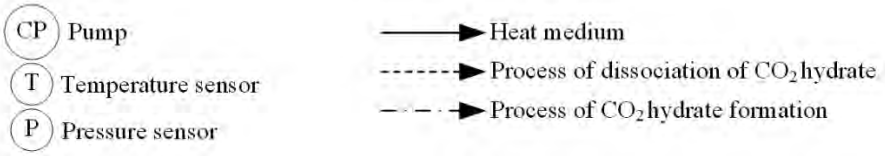

Fig. 7 Diagram showing heat transfer in a GHB

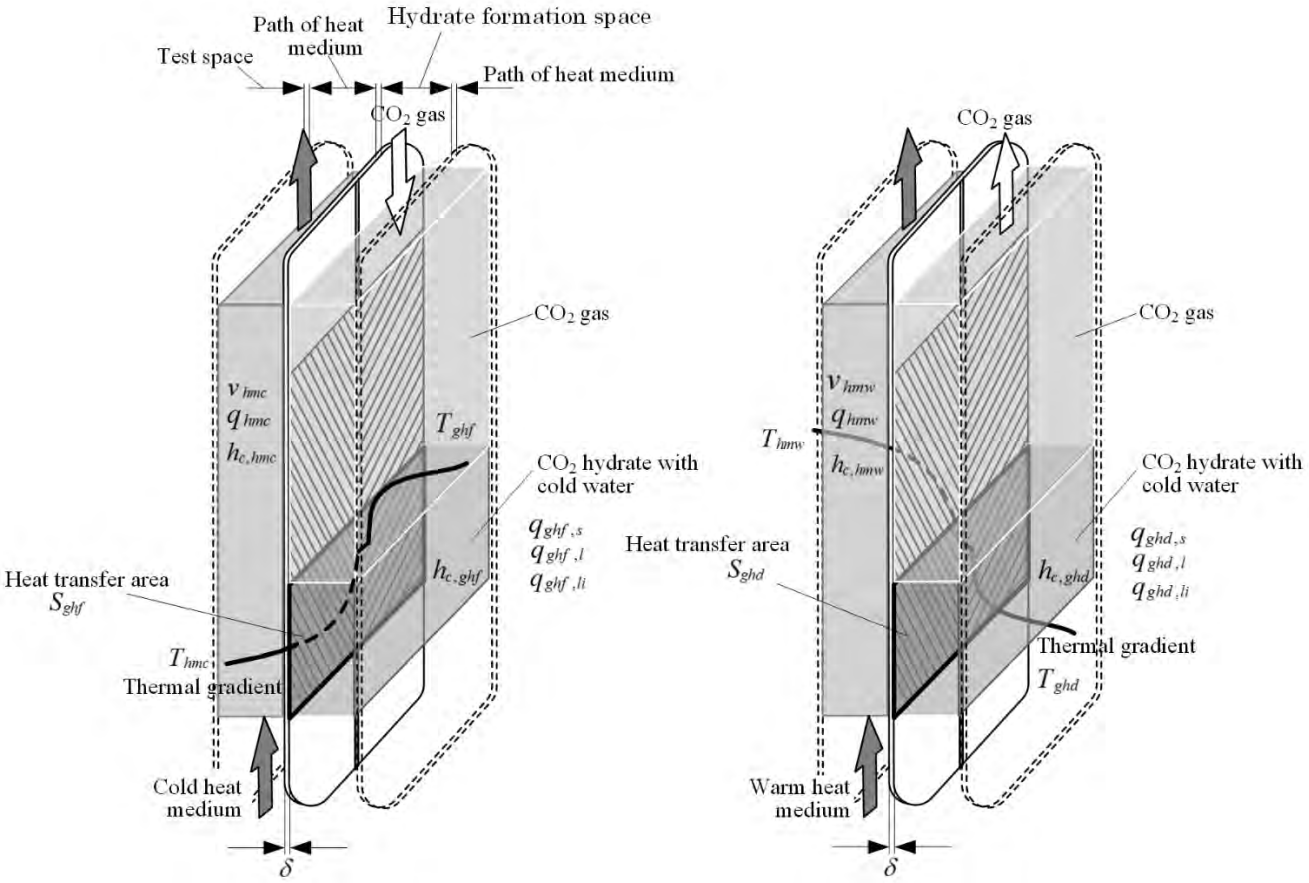

Fig. 8 Graph showing hourly air temperature for five representative days during November 2012 to March 2013 in Kitami, Japan

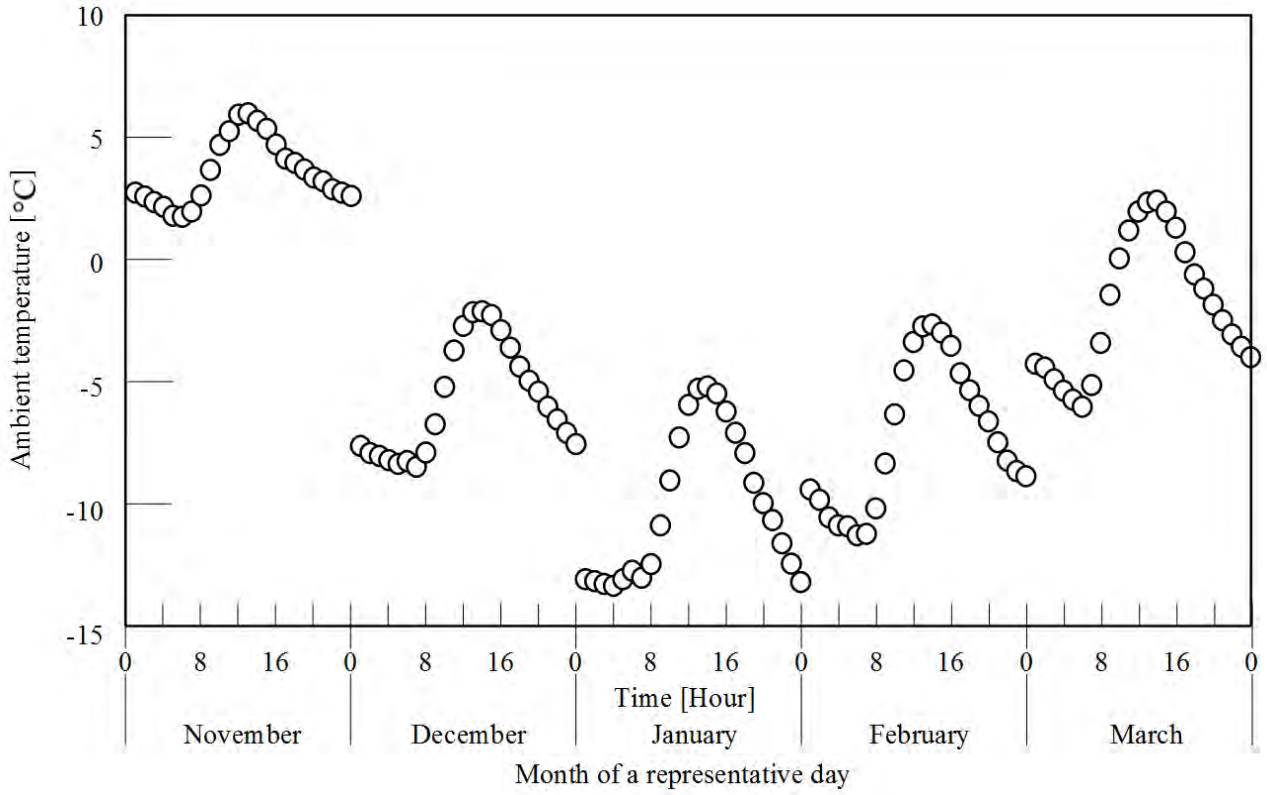

Fig. 9 Graphs showing electricity demand and heat load in kW versus time during one day for individual houses in Kitami

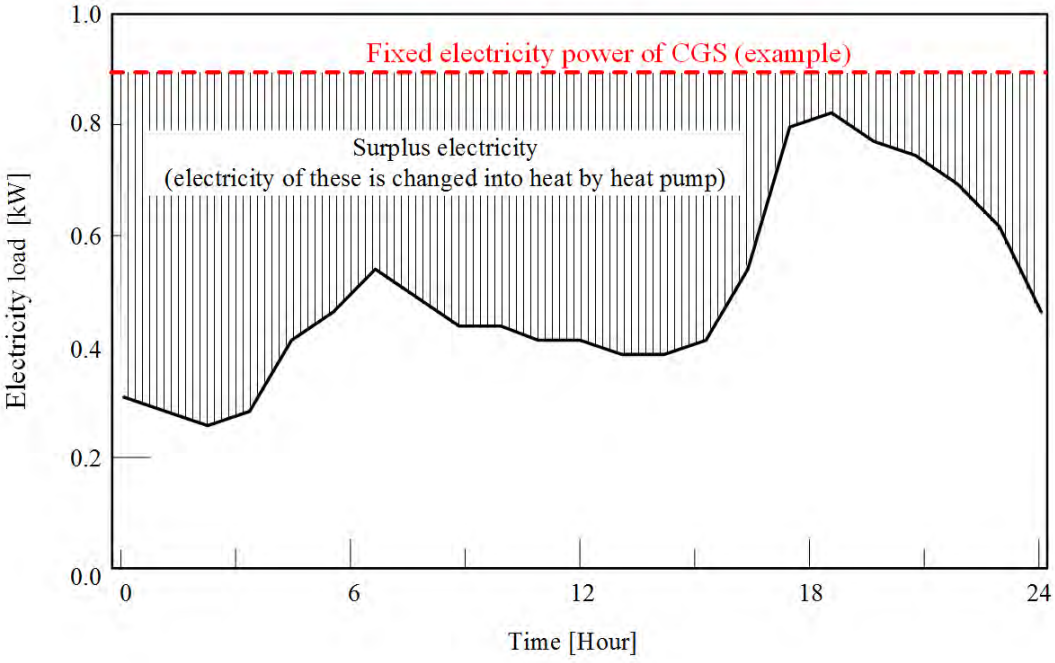

(a) Electricity load

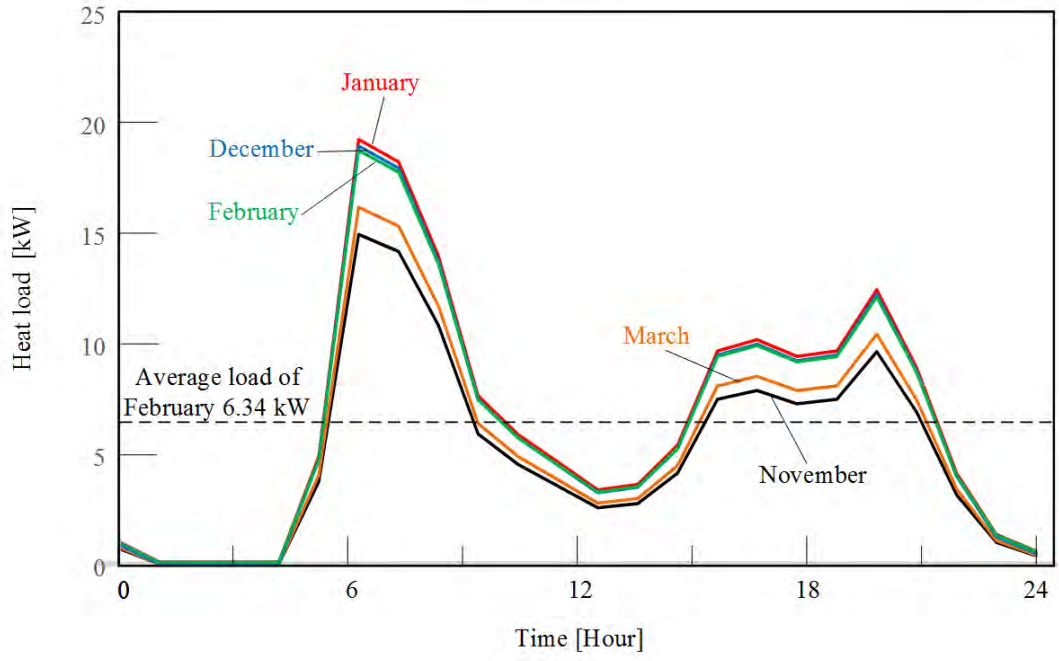

(b) Heat load

Fig. 10 Calculation flow for analyzing the operation of a small-scale CGS paired with a GHB installed in a house in a cold region

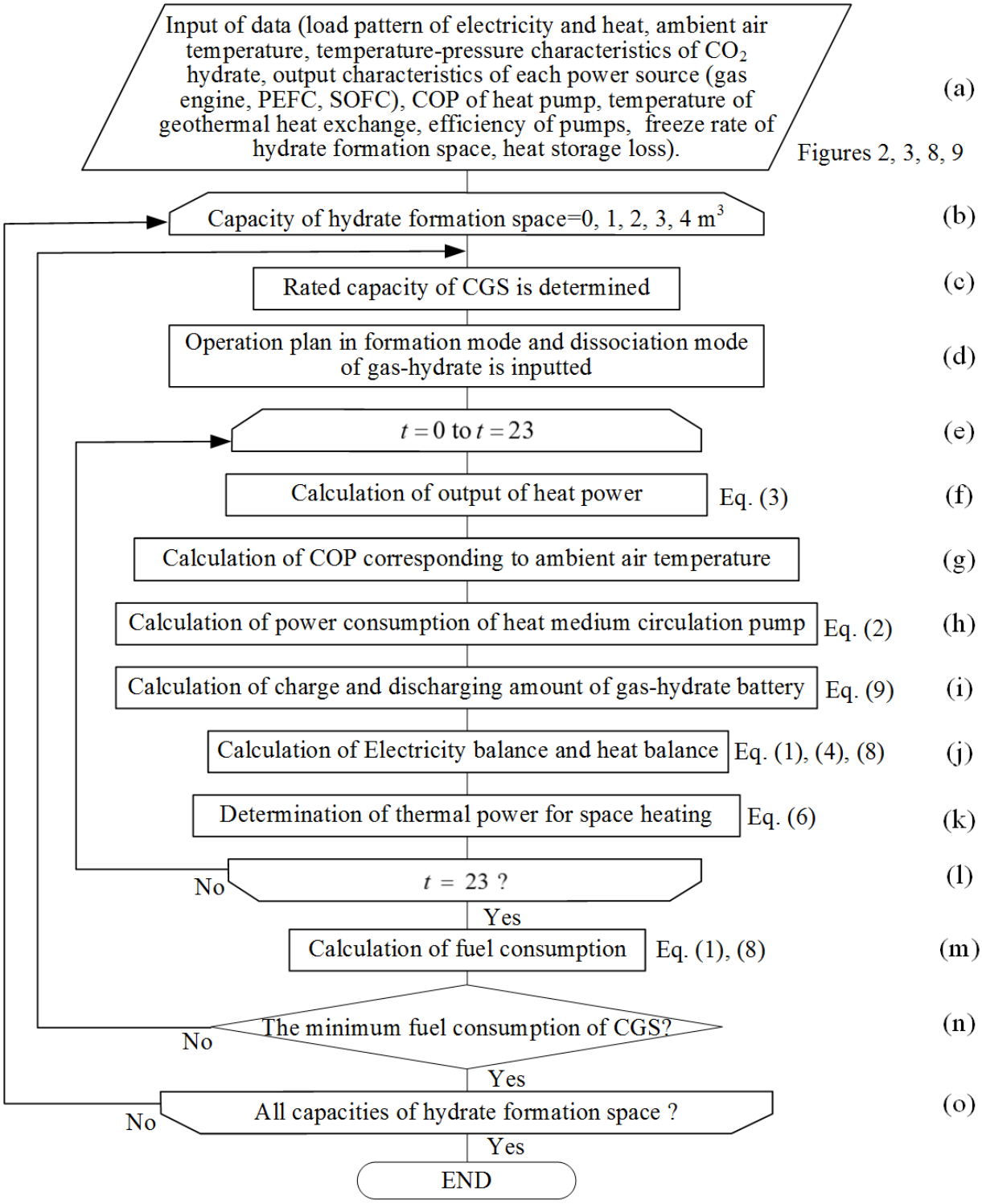

Fig. 11 Graphs of internal pressure versus time for gas hydrate formation–dissociation experiments. The experiments tested the efficacy of adding a catalyst to the reaction space.

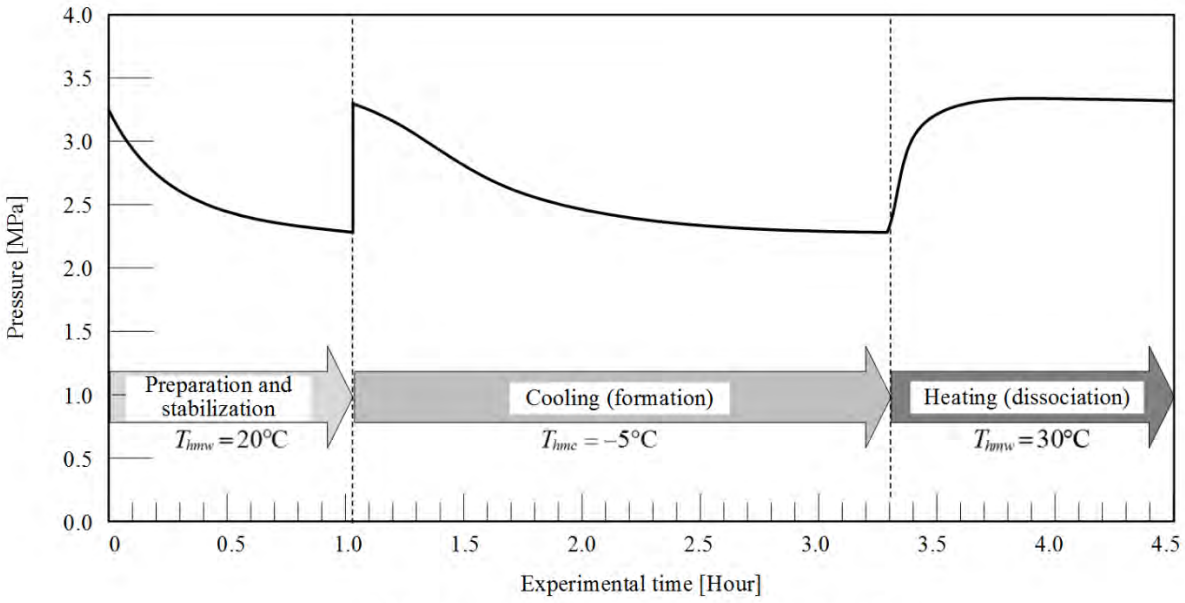

(a) Conventional method test without catalyst

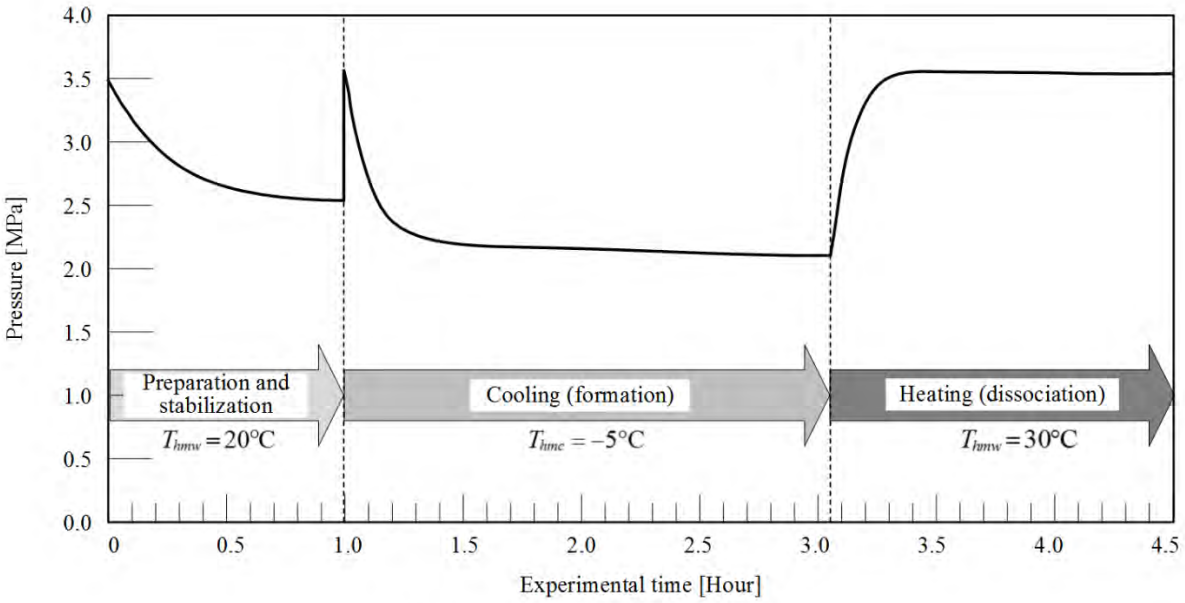

(b) Test using iron oxide–carbon catalyst

Fig. 12 Graphs showing heat and electric load and output for a basic cogeneration power system during one day

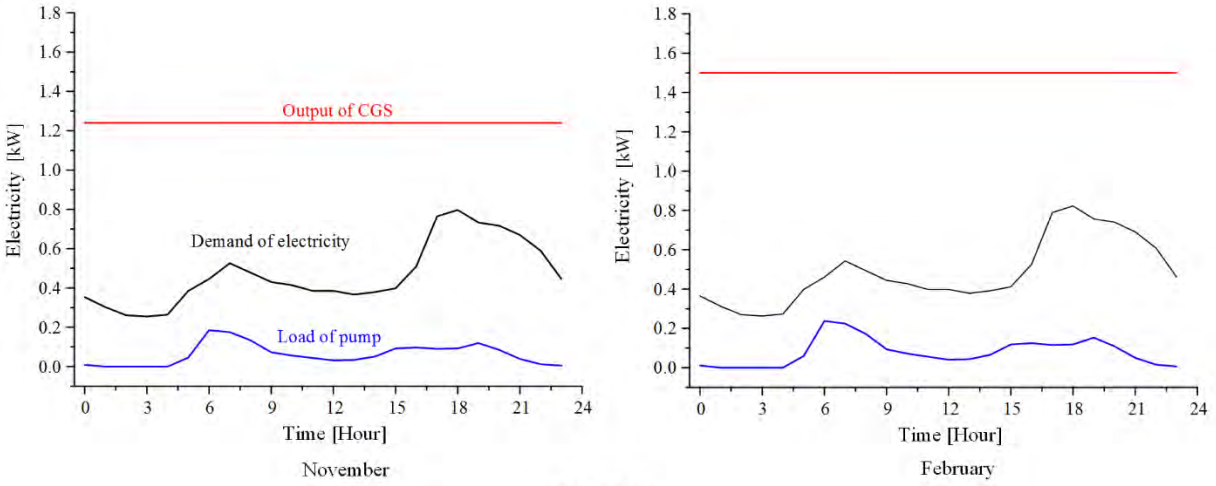

(a) Electricity

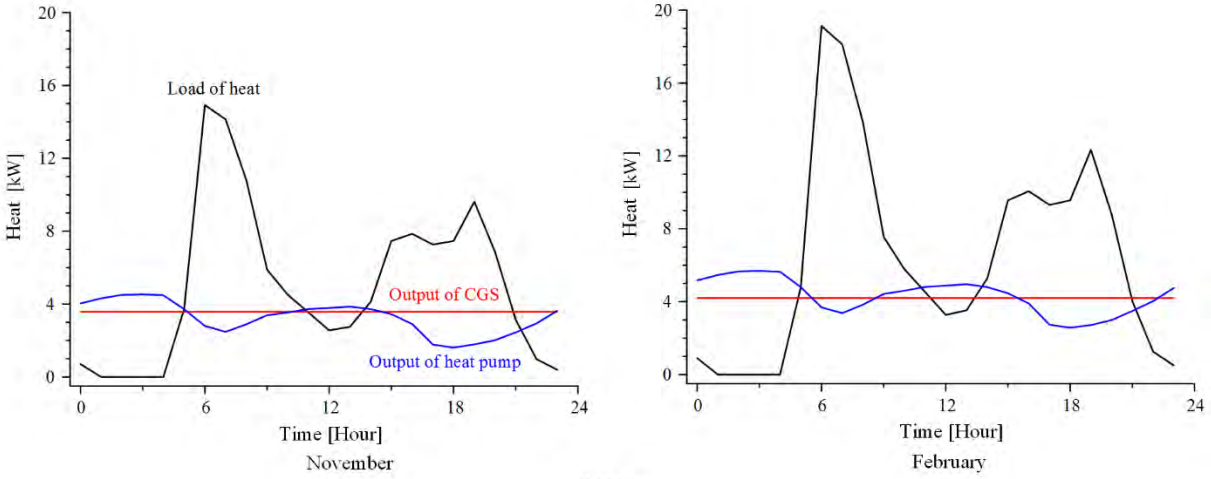

(b) Heat

Fig. 13 Graphs showing the results from a computer simulated operation of a gas engine-powered CGS for one day

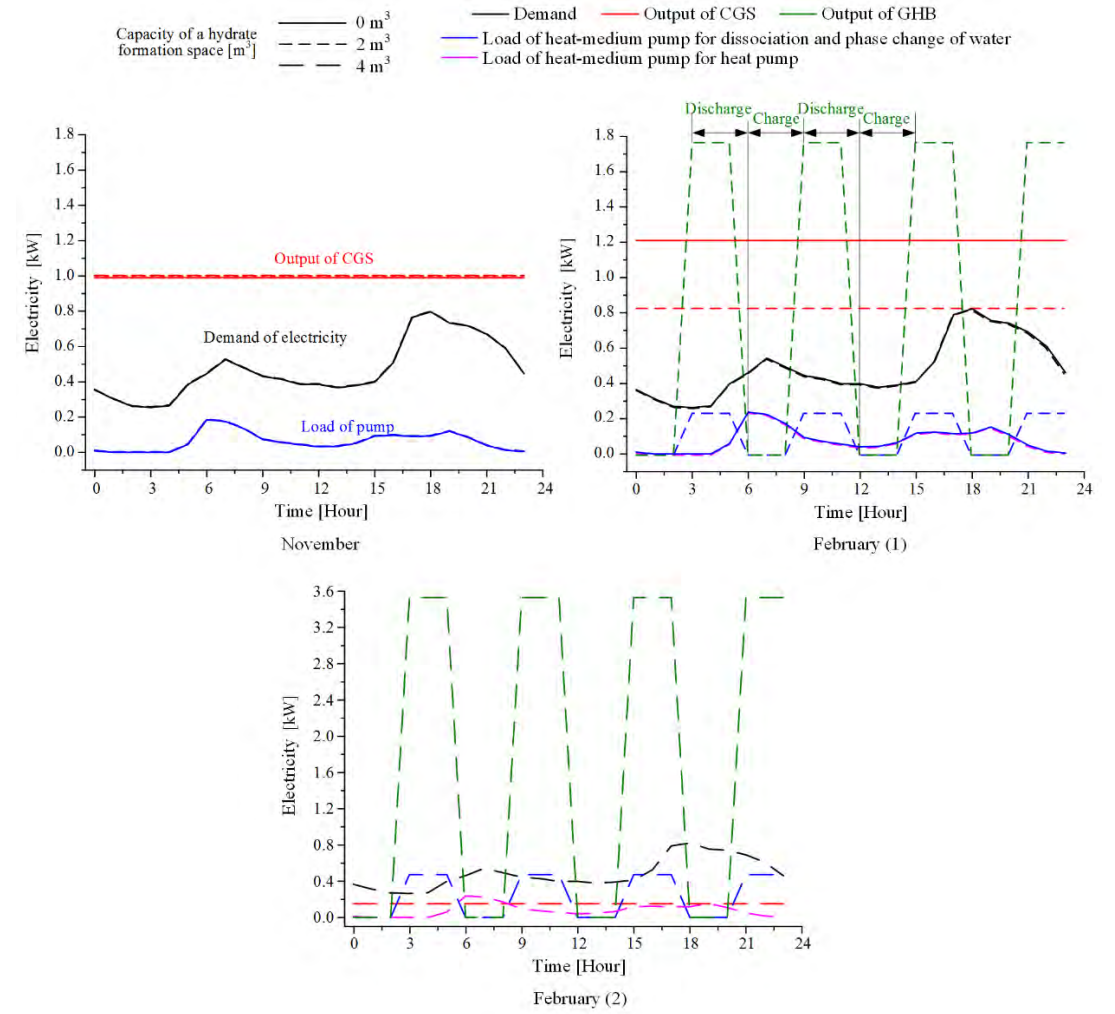

(a) Electricity

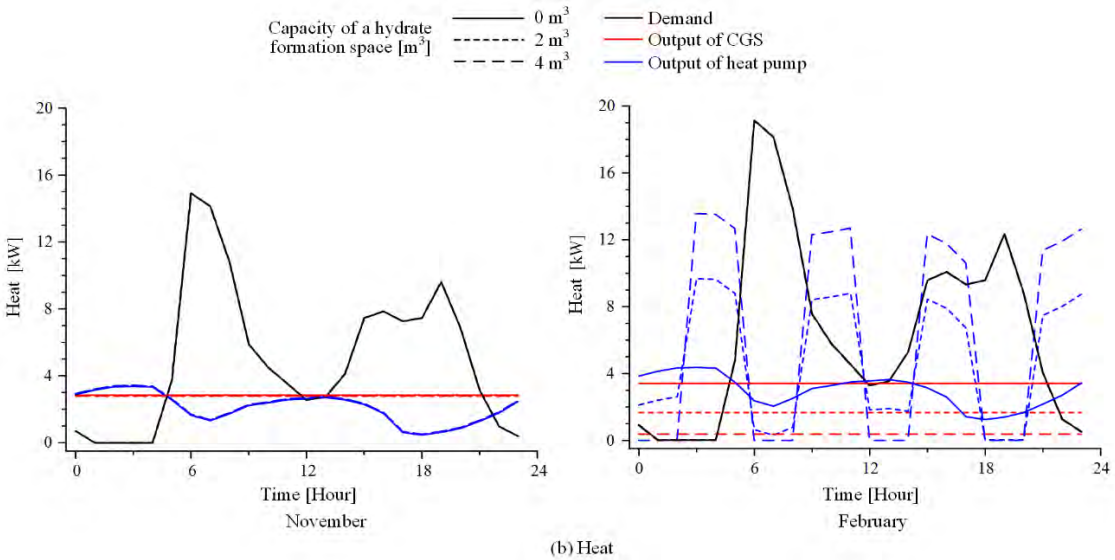

(b) Heat

Fig. 14 Analysis results of power equipment operation for PEFC CGS

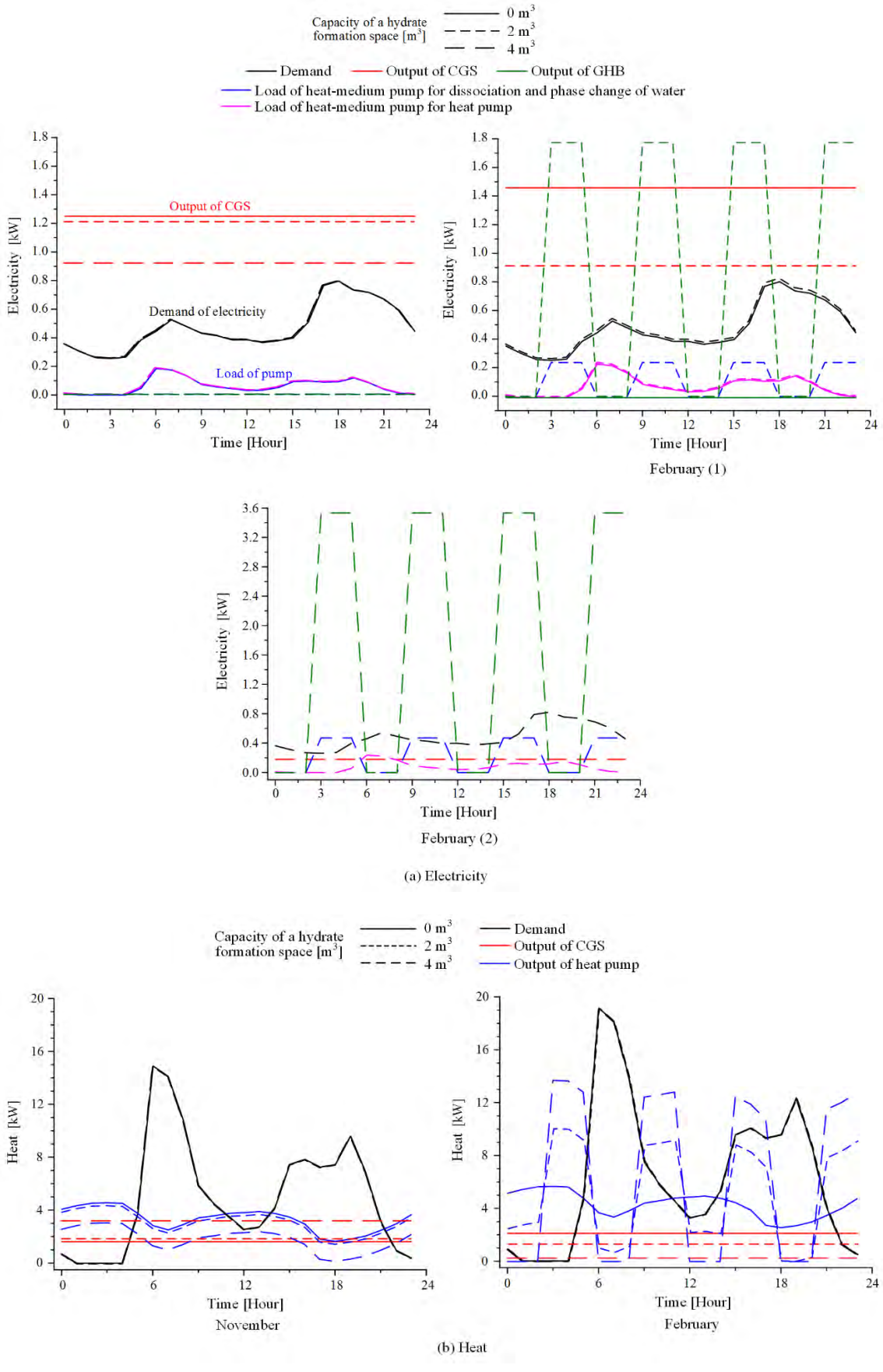

Fig. 15 Analysis results of power equipment operation for SOFC CGS

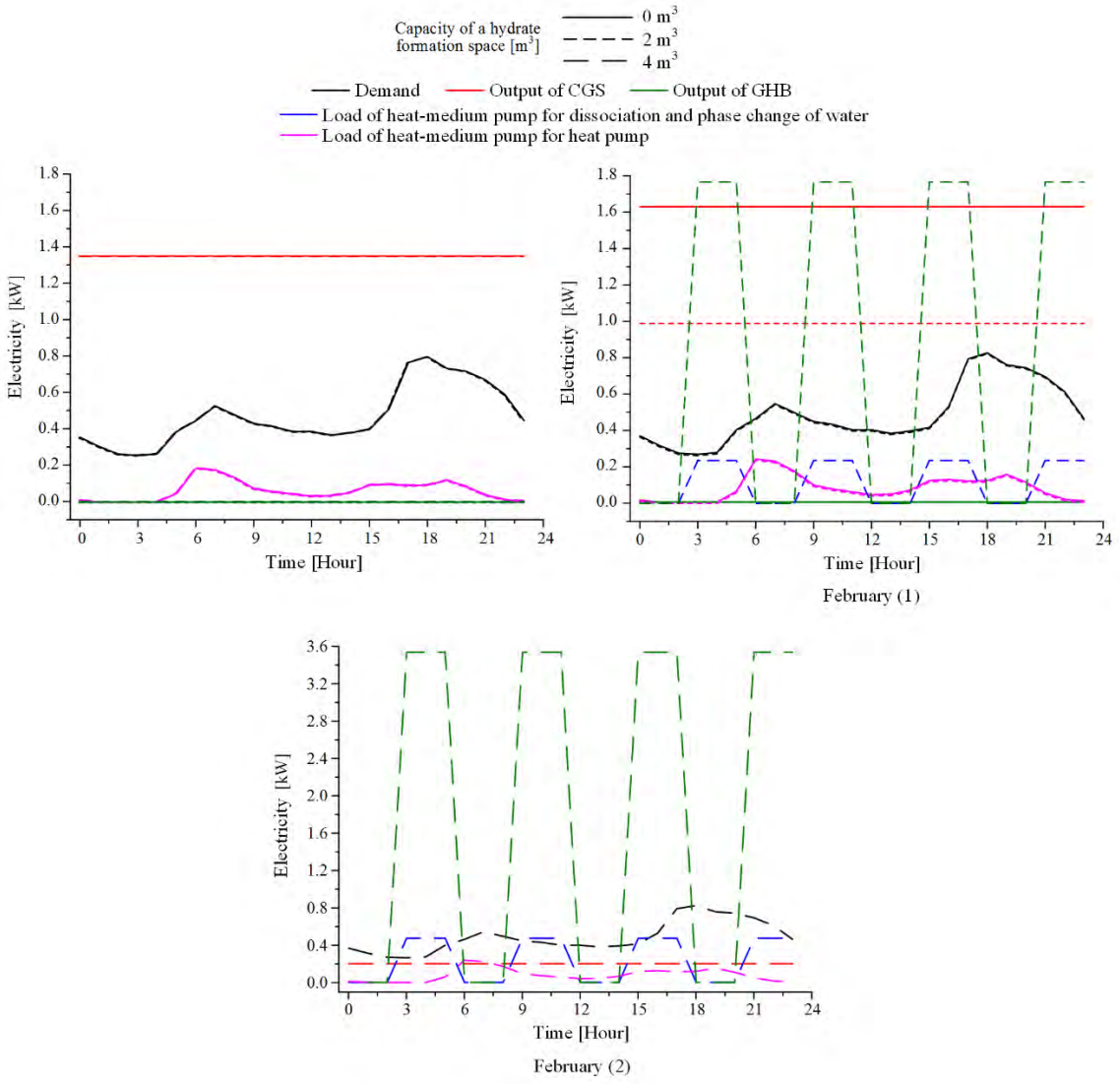

(a) Electricity

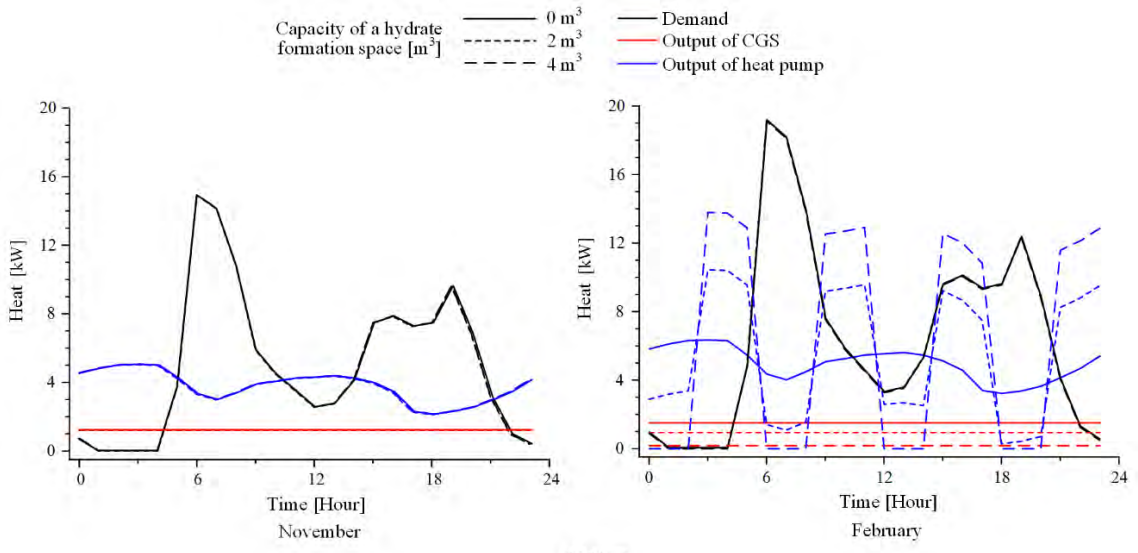

(b) Heat

Fig. 16 Graphs showing monthly performance of the basic system during November 2012 to March 2013

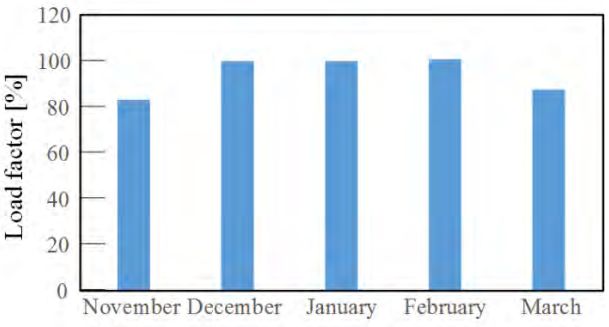

(a) Load factor

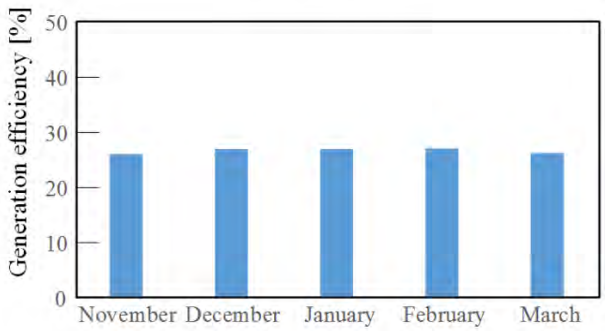

(b) Generation efficiency

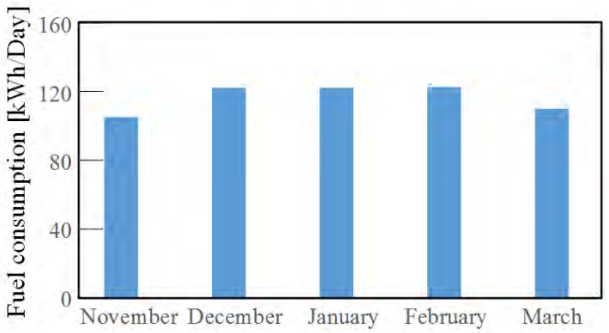

(c) Fuel consumption

Fig. 17 Graphs showing total monthly load factors, generation efficiency, and fuel consumption for three types of CGSs for the period November 2012 to March 2013.

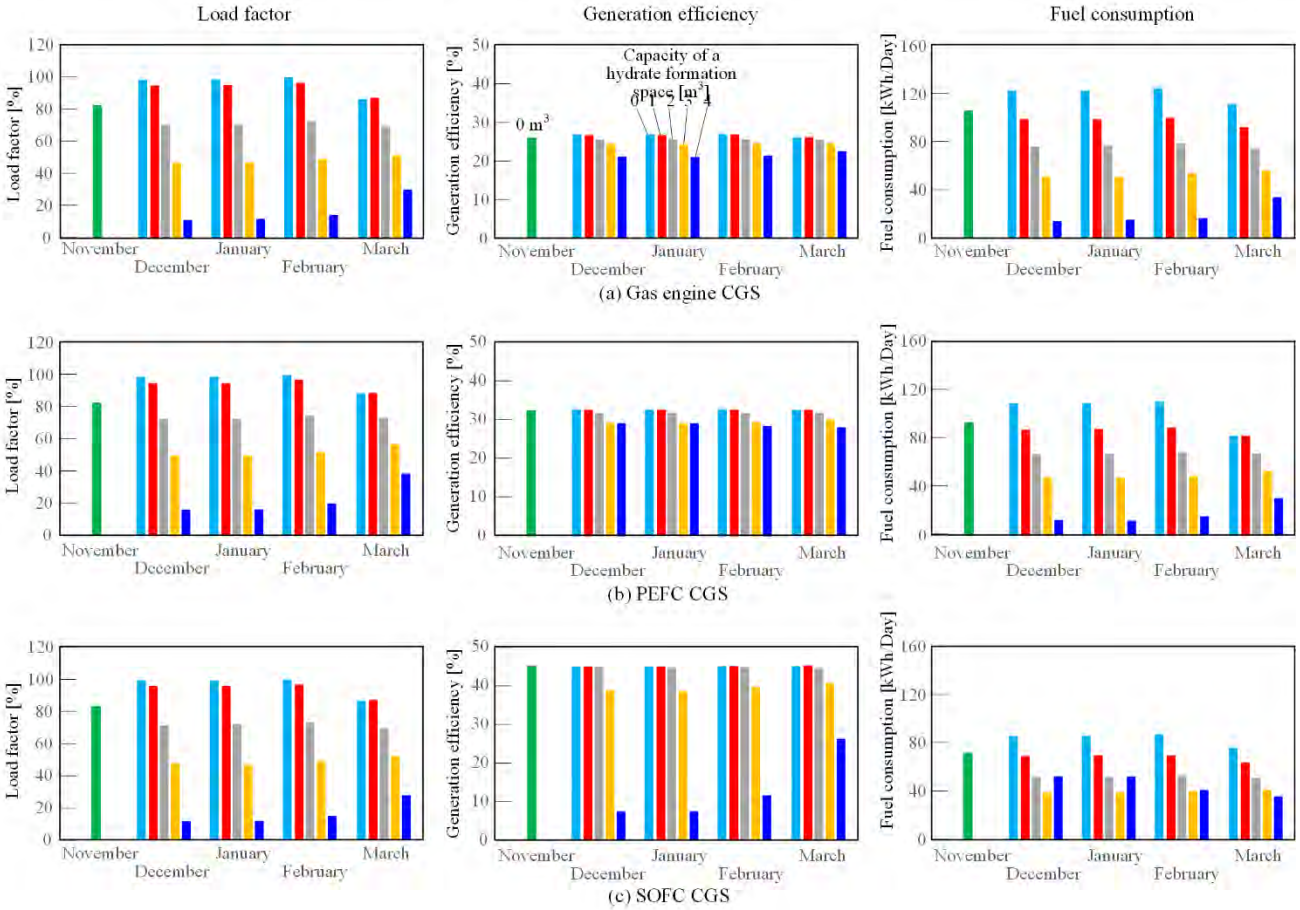

Fig. 18 Graphs showing the source of electric and heat energy for the five representative days for the basic CGS

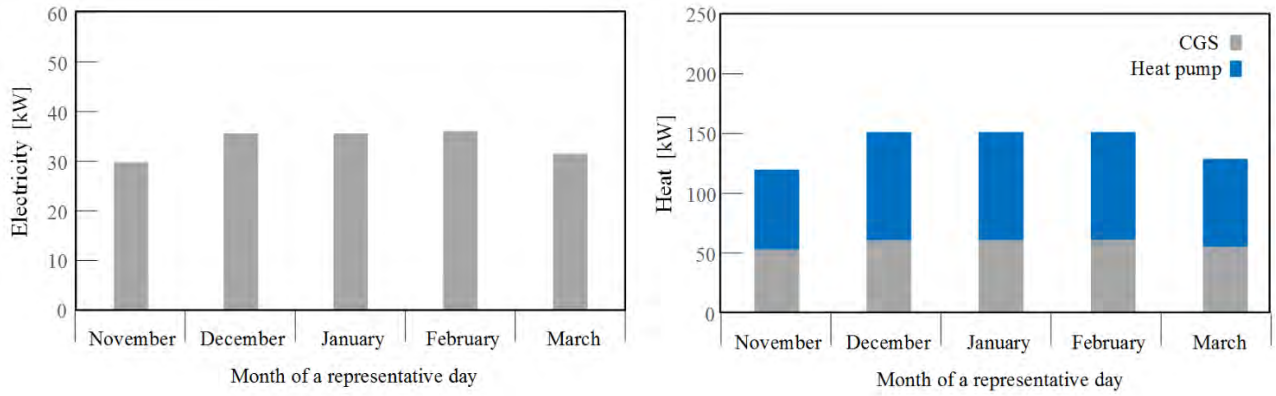

(a) Electricity

(b) Heat

Fig. 19 Composition of energy outputs by each CGS

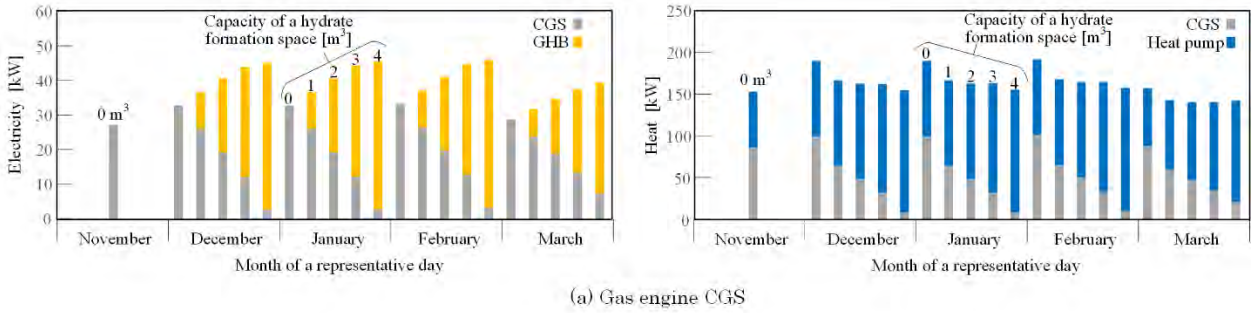

(a) Gas engine CGS

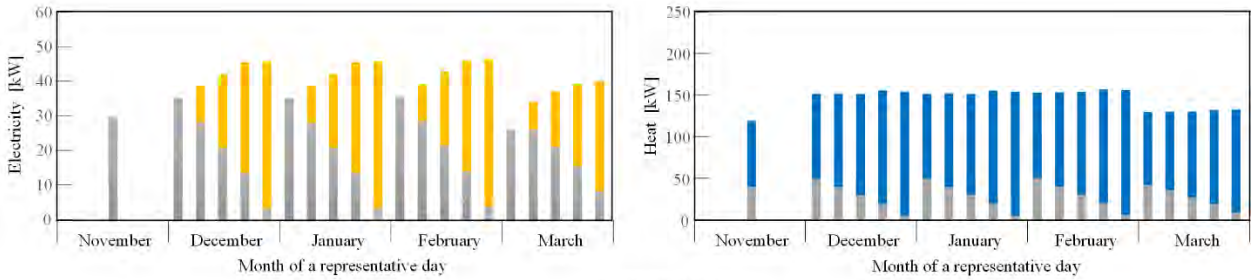

(b) PEFC CGS

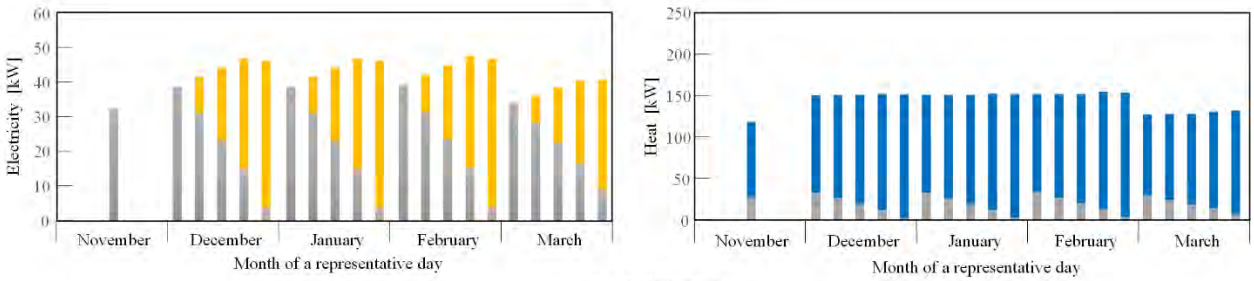

(c) SOFC CGS

Fig. 20 Relation between heat to power ratio and fuel consumption for each system. Capacity of 0 to 4 m^3 of hydrate formation space.